Topochemical Fluorination of $LaBaInO_4$ to $LaBaInO_3F_2$, their Optical Characterization and Photocatalytic Activities for Hydrogen Evolution

Shama Perween[*,a,b], *Kerstin Wissel*[a], *Zsolt Dallos*[c,d], *Morten Weiss*[e], *Yuji Ikeda*[f], *Sami Vasala*[g], *Sabine Strobel*[h], *Peter Schützendübe*[i], *Pascal M. Jeschenko*[j], *Ute Kolb*[c,d], *Roland Marschall*[e], *Blazej Grabowski*[f] *and Pieter Glatzel*[g]

[*,a]Institute for Materials Science, Materials Synthesis Group, University of Stuttgart, Heisenbergstrasse 3, 70569 Stuttgart, Germany.
[b]Institute for Materials Science, Technical University of Darmstadt, Alarich-Weiss-Straße 2, 64287 Darmstadt, Germany.
[c]Institute for Applied Geosciences, Technical University of Darmstadt, Schnittspahnstrasse 9, 64287 Darmstadt, Germany.
[d]Institute of Inorganic Chemistry and Analytical Chemistry, Johannes Gutenberg-University of Mainz, Duesbergweg 10-14, 55128 Mainz, Germany.
[e]Department of Chemistry, University of Bayreuth, Universitätsstrasse 30, 95447 Bayreuth, Germany.
[f]Institute for Materials Science, Department of Materials Design, University of Stuttgart, Pfaffenwaldring 55, 70569 Stuttgart, Germany.
[g]ESRF - The European Synchrotron, 71 Avenue des Martyrs, 38000 Grenoble, France.
[h]Institute of Inorganic Chemistry, University of Stuttgart, Pfaffenwaldring 55, 70569 Stuttgart, Germany.
[i]Max Planck Institute for Intelligent Systems, Stuttgart D-70569, Germany.
[j]Max Planck Institute for Medical Research, D-69120, Heidelberg, Germany.

*Corresponding Author
Email: shama.perween@imw.uni-stuttgart.de

KEYWORDS

Ruddlesden–Popper, Oxyfluoride $LaBaInO_3F_2$, Automated Diffraction Tomography, X-ray Absorption Spectroscopy, Photocatalytic Hydrogen Evolution.

ABSTRACT

We report on a non-oxidative topochemical route for the synthesis of a novel indate-based oxyfluoride, $LaBaInO_3F_2$, using a low-temperature reaction of Ruddlesden–Popper-type $LaBaInO_4$ with polyvinylidene difluoride as a fluorinating agent. The reaction involves the replacement of oxide ions with fluoride ions as well as the insertion of fluoride ions at interstitial sites. From the characterization via powder X-ray diffraction (PXRD) and Rietveld analysis as well as automated electron diffraction tomography (ADT) it is deduced that the fluorination results in a symmetry lowering from *I4/mmm* (139) to monoclinic *C2/c* (15) with an expansion perpendicular to the perovskite layers and a strong tilting of the octahedra in the *ab* plane. Disorder of the anions on the apical and the interstitial sites seems to be favored. The most stable configuration for the anion ordering is estimated based on an evaluation of bond distances from the ADT measurements via bond valence sums (BVSs). The observed disordering of the anions in the oxyfluoride results in changes of the optical properties and thus shows that the topochemical anion modification can present a viable route to alter optical properties. Partial densities of states (PDOSs) obtained from *ab initio* density functional theory (DFT) calculations reveal a bandgap modification upon fluoride-ion introduction which originates from the presence of the oxide anions on the interstitial sites. The photocatalytic performance of the oxide and oxyfluoride shows that both of the materials are photocatalytically active for hydrogen (H_2) evolution.

1. INTRODUCTION

The development of energy-harvesting and energy-storage devices is a key challenge to meet the requirements of a sustainable energy supply. Energy storage is important to establish the transition from fossil fuels to reliable renewable energies.[1] Harvesting the abundantly available solar energy and converting it into required energy forms, such as electricity or chemical energy, lies at the core of sustainable energy research.[2] The photocatalytic approach is one of

the greenest ways to harvest solar energy and directly generate hydrogen by using a photocatalyst.[3, 4]

In photocatalysis, a semiconductor absorbs light and thereby generates charge carriers that can catalyze redox reactions at the surface.[5] An optimal photocatalyst for hydrogen formation from water should exhibit high stability, broad visible-light absorption, and low electron–hole (e^-–h^+) recombination rates.[6] Recently, significant efforts have been put forward to design new functional materials suitable for photocatalysis. Perovskites, layered perovskites, and derivatives are promising photocatalysts due to their excellent structural properties and compositional flexibility.[7, 8] Among the various perovskite-related phases, Ruddlesden–Popper–type (RP) phases have attracted particular interest because of their superior photocatalytic activity, visible-light response, and unique optical and electronic properties.[8, 9]

The RP series $A_{n+1}B_nO_{3n+1}$ (for n = 1 also referred to as K_2NiF_4-type structure) can be understood as being built of alternating perovskite ABO_3 layers of thickness n and rock salt type AO-layers.[10] The highest symmetry of these phases is $I4/mmm$. At least two distinguishable crystallographic sites exist for anions (labelled X in the following), i.e., equatorial ($X1_{(eq)}$, *4c*) and apical ($X2_{(ap)}$, *4e*) anion sites (**Figure 1**). Depending on the B-site metal and its stability in different oxidation states (as encountered for d- or p-block elements), many RP-type compounds possess the flexibility to deviate from their stoichiometric anion composition. The flexibility originates from the presence of large interstitial anion sites ($X3_{(int)}$, *4d*) within the rock salt-type layers.[11] Due to this flexibility, compounds with multiple types of anions can be prepared. If the interstitial sites are fully filled by oxide ions, the respective compound possesses the Aurivillius-type structure, as found, for example, in Bi_2WO_6.[12] It is also possible to fill the interstitial sites with fluoride ions. This has been demonstrated by our research group for $LaSrMnO_4$,[11] La_2CoO_4,[13] and La_2NiO_4[14] via electrochemical and

topochemical methods, which are required due to the metastability of such oxyfluoride phases. Apart from oxidative fluoride ion insertion, it is also possible to substitute one oxide ion by two fluoride ions (substitution of one oxide ion by one fluoride ion and an additional intercalation of one fluoride ion in an interstitial site), leading to $A_{n+1}B_nO_{3n+1-x}F_{2x}$ with $0 < x \leq 2$.[15, 16] Such substitutive topochemical fluorination reactions can be performed with fluoride-containing polymers, e.g., polyvinylidene difluoride (PVDF, $(CH_2CF_2)_n$)[16, 17] with *n* denoting the number of monomers.

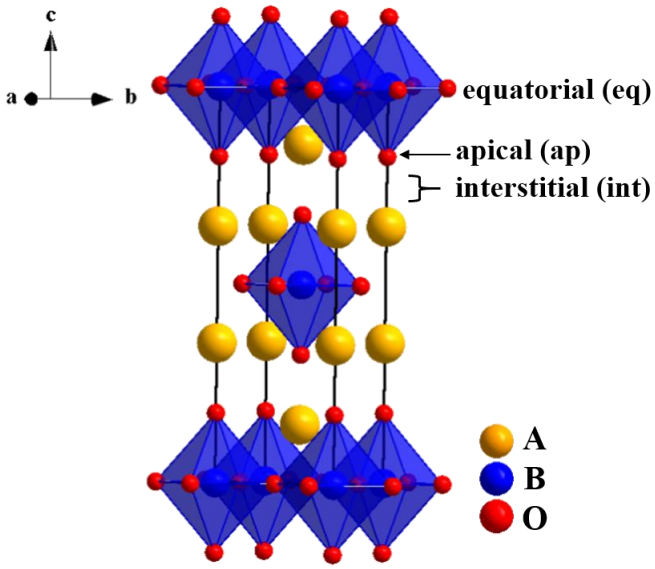

Figure 1 *General schematic of the Ruddlesden–Popper structure $A_{n+1}B_nO_{3n+1}$ (n = 1) with equatorial (eq) and apical (ap) anion sites, and space for interstitial (int) anion sites within the rock salt layers.*

A few RP-type materials such as strontium titanate (Sr_2TiO_4), alkaline earth metal-lanthanum-titanate ($AELa_4Ti_4O_{15}$, AE = Ca/Sr/Ba), lithium calcium-tantalates ($Li_2CaTa_2O_7$), and strontium tin oxides (Sr_2SnO_4) have been reported to be efficient hydrogen evolution catalysts with bandgaps of 3.52 eV, 3.79–3.85 eV, 4.36 eV, 4.6 eV, respectively.[3, 7, 9, 18] The wide bandgaps impose limitations, specifically these compounds are active in UV light only and thus not sustainable enough to harvest solar energy. Indium-based compounds such as $AInO_2$ (A = Ag, Na, Li), and $AEIn_2O_4$ (AE = Ca, Sr, Ba) are also known as photocatalysts.[19] Indeed, indate based oxide materials[3, 20] are of interest for a range of functional properties due to their optical

features.[21] Though more complex indates are known to exist in the RP-type structure with a general formula of $LnAEInO_4$ (Ln = lanthanides, Y; AE = alkaline earth metals[22]), their photocatalytic properties have not been reported so far.

Within the present study, we report on the synthesis of the RP phase oxide material $LaBaInO_4$ and its oxyfluoride counterpart $LaBaInO_3F_2$ via topochemical fluorination. Topochemical fluorination of the oxide material with PVDF leads to a transformation of the crystal structure from body-centered tetragonal to *C*-centered monoclinic symmetry with a disordered anion sublattice. The transformation has a significant impact on the optical properties, which we analyze by density functional theory (DFT) calculations. Photocatalytic performance reveals that both compounds, $LaBaInO_4$ and $LaBaInO_3F_2$, are photocatalytically active in sacrificial H_2 evolution.

2. EXPERIMENTAL

2.1 Materials & Synthesis Method

$LaBaInO_4$ and $LaBaInO_3F_2$: The RP-type phase $LaBaInO_4$ was synthesized by using a solid-state reaction method. La_2O_3 (Alfa Aesar, 99.9%) dried at 1100 °C for 3 h, In_2O_3 (Alfa Aesar, 99.9%), and $BaCO_3$ (Alfa Aesar, 99%) were used. Stoichiometric amounts of the starting materials were mixed using a planetary ball mill (ZrO_2 grinding jar and balls at 600 rpm for 1 h) and calcined twice at 1300 °C for 24 h in air with a heating and cooling rate of 2 °C min^{-1} and with an intermediate homogenization with mortar and pestle. For the topochemical fluorination of $LaBaInO_4$ to $LaBaInO_3F_2$, the oxide was hand-milled with the fluorinating agent poly(vinylidene fluoride) $(CH_2CF_2)_n$ (PVDF; Sigma-Aldrich) in a molar ratio of 1:1 (in the given chemical equation below: $x = 1$ corresponds to 2 F per $LaBaInO_4$ unit) and heated at 370 °C for 24 h in air with a heating and cooling rate of 2 °C min^{-1}.[16, 17] The chemical equation for this process is given by

$$\mathbf{LaBaInO_4} + \boldsymbol{x/n}\mathbf{(CH_2CF_2)_n} + \mathbf{2}\boldsymbol{x}\ \mathbf{O_2} \xrightarrow{\Delta} \mathbf{LaBaInO_{4-x}F_{2x}} + \mathbf{2}\boldsymbol{x}\ \mathbf{CO_2} + \boldsymbol{x}\ \mathbf{H_2O}$$

2.2 Characterization

2.2.1 Powder X-ray diffraction (PXRD)

Powder X-ray diffraction (PXRD) patterns were recorded on a Rigaku SmartLab diffractometer with a wavelength λ of 1.540596 Å in an angular range of 2θ from 10° to 130° with a scan speed of 0.4°/min and 0.005°/step in Bragg−Brentano geometry with Cu radiation ($K_{\alpha1}$ and $K_{\alpha2}$ with an intensity ratio of 2:1) with a HyPix-3000 detector. Analysis of diffraction data was performed using the Rietveld method with the program TOPAS V 6.0[23] on the whole 2θ range. The instrumental intensity distribution was determined by using a reference scan of LaB_6 (NIST 660a). The microstructural parameters (crystallite size and strain broadening) were refined to adjust the peak shapes. Different isotropic thermal parameters were refined for the different crystallographic sites.

2.2.2 Attenuated Total Reflection-Fourier Transform Infrared (ATR-FTIR) spectroscopy and Thermogravimetric analysis (TGA)

FTIR spectroscopy measurements were done by using ATR-FTIR, BRUKER TENSOR II. ATR-FTIR involves the collection of radiation reflected from the interfacial surface between the sample and a reflection element (ATR crystal). Evanescent waves emanate from the crystal and penetrate the sample.[24] The measurements were recorded from 400-4000 cm^{-1} range at ambient condition.

Thermogravimetry analysis (TGA) was performed under argon atmosphere on an STA 449 F3 System (Netzsch-Gerätebau GmbH, Selb, Germany) with a silicon carbide furnace, TG-DSC sample holder system and type S thermocouple. Heating and cooling rates were 10 $K.min^{-1}$. For the measurement, 23.9 mg and 14.2 mg were used for $LaBaInO_4$ and $LaBaInO_3F_2$,

respectively. The aged samples stored at ambient conditions were used for ATR-FTIR as well TGA measurements.

2.2.3 Transmission Electron Microscopy Characterization and Automated Diffraction Tomography (ADT)

A powdered sample of $LaBaInO_3F_2$ was dispersed in *n*-hexane using an ultrasonic bath and sprayed on a carbon-coated copper grid using an ultrasound sonifier for electron dispersive X-ray spectroscopy (EDX) and automated electron diffraction tomography (ADT) studies. Measurements were carried out with a FEI TECNAI F30 S-TWIN transmission electron microscope equipped with a field emission gun and working at 300 kV. For fast and automated diffraction tomography (Fast-ADT)[25] experiments, a 10 μm condenser aperture, spot size 8, and gun lens 6 were set to produce a quasi-parallel beam of 200 nm in size. Scanning transmission electron microscopy (STEM) images were collected using a Fischione high-angle annular dark-field (HAADF) detector. Electron diffraction patterns were acquired with an UltraScan4000 charge-coupled device (CCD) camera provided by Gatan (16 bit, 4096 × 4096 pixels). Hardware binning 2 and an exposure time of 2 seconds were used for the acquisition. Fast-ADT data sets were acquired with an automated acquisition module developed for FEI and JEOL microscopes, which allows the acquisition of electron diffraction tomography in around 10 min for conventional CCD cameras and a fixed-tilt step of 1°. Precession electron diffraction (PED) was coupled to the Fast-ADT data collection to minimize the dynamical effects and improve the reflection intensity integration quality. PED was generated utilizing the DigiStar system developed by NanoMegas SPRL and it was kept to 1°. Three-dimensional processing of the Fast-ADT data was analyzed by the eADT[26] software package. Sir2014[27] was used for the *ab initio* structure solution, and Jana2006 was later used for crystal structure refinement. Intensity extraction for the dynamical refinement was done by Jana2020.[28]

2.2.4 X-ray Absorption Spectroscopy (XAS)

High-energy-resolution fluorescence detected X-ray absorption spectra (HERFD-XAS) at the indium L_3 edge were measured at the beamline ID26 of the European Synchrotron Radiation Facility (ESRF) in Grenoble, France. The incident energy was selected by the Si(111) reflection of a double crystal monochromator. The intensity of the indium $L_{\alpha 1}$ (L_3-M_5) emission energy (3.287 keV) was recorded using a point-to-point, in-vacuum Johansson emission spectrometer.[29] Seven Si analyzer crystals oriented in (220) (Saint-Gobain, France) reflection were used to select the emission energy, together with a multi-wire gas proportional counter. The intensity was normalized to the incident flux and the spectra were normalized to the spectral area. The samples were mixed in a 1:1 ratio with cellulose and pressed into pellets before measurement.

2.2.5 Optical Characterization

UV-Visible diffuse reflectance spectroscopy (UV-Vis DRS) of the synthesized compounds was recorded in the wavelength range of 240–2000 nm (5.2–0.6 eV) at room temperature on a J&M TIDAS UV-Vis-NIR spectrophotometer equipped with a reflection measuring head. As reference a $BaSO_4$ standard was used. By applying the Kubelka–Munk (K–M) function, we determined the optical band gaps for these compounds employing linear fits of the detected curves. Using the K–M relation,[30] the reflectance (R_α) is converted into absorbance via the K–M function ($F(R_\alpha)$) which is given by $F(R_\infty) = (1 - R_\infty)^2/2R_\infty$. In this present study, a direct 'Energy vs Absorbance' plots were determined.

For photoluminescence (PL) spectroscopy, the synthesized compounds were dispersed in acetone and sonicated for 5 min at room temperature. The obtained slurry (40 µL) was deposited on a cleaned silicon wafer to obtain a thin film deposition and dried at room temperature for 2 h. The silicon wafers (10×10 mm^2) were cleaned by consecutive sonication

in deionized H_2O and acetone with subsequent extensive washing prior to the deposition of the sample. PL measurements were performed at room temperature. The emission spectra were recorded with the spectrofluorometer Spex FluoroLog 3, Horiba Jobin Yvon, Germany.

2.2.6 Scanning Electron Microscopy (SEM)

Scanning electron microscopy (SEM) images of the calcined samples were taken by using the secondary electron detector of a Philips XL30 FEG scanning electron microscope operating at 30 KeV accelerating voltage. To prevent the samples from charging, a thin gold coating of 10 nm was sputtered prior to the measurements.

2.2.7 X-ray Photoelectron Spectroscopy (XPS)

The X-ray photoelectron spectroscopy (XPS) measurements were carried out in a Thermo VG Thetaprobe system (Thermo Fisher Scientific, USA). The monochromatic X-ray source produced an Al Kα radiation ($h\nu$ = 1486.68 eV) with an electrical power of 100 W. The probed excitation circle on the sample was 400 µm. The base pressure of the XPS analysis chamber was 3×10^{-10} mbar. For all measurements a survey measurement was taken with a pass energy of 200 eV and 5 scans. The used dwell time was 50 ms and the step width 0.2 eV. For all single scan measurements, we used the instrument's snap scan mode with 500 scans, each 1 sec. The measurements were fitted using the fitting routines included in the XPS software Advantage. Here we used the Powell-fitting algorithm and the smart-Background subtraction. The calibration of the measured binding energy was done and periodically proved with a silver calibration sample. The measured peak position was compared to the nominal one.

2.2.8 Experimental Evaluation of Photocatalytic Hydrogen Evolution

Photocatalytic hydrogen evolution experiments were performed with both $LaBaInO_4$ as well as $LaBaInO_3F_2$ to investigate the photocatalytic activities of the materials synthesized. For this purpose, 40 mg powder samples of each compound were dispersed in a mixture of 550 mL DI-

H_2O and 50 mL ethanol, ultrasonicated for 10 minutes before filling into the reactor at a temperature of 10 °C (Lauda Proline RP845) and a gas flow rate of 100 mL/min Ar 5.0 (Bronkhorst El-Flow Select). A double-walled glass reactor with a double-walled borosilicate inlet was used for the housing of the lamp. A non-continuous iron-doped Hg light source with 500 W power was used as a lamp (TQ718-Z4 Peschl Ultraviolet). The samples were stirred during the reaction process. Gas evolution was measured with a quadrupole mass spectrometer (HPR-20 Q/C Hiden Analytical), with one data point being collected approximately every 60 seconds. An aqueous solution of H_2PtCl_6 (Aldrich) was added through a septum using a syringe before the lamp was started, resulting in in-situ photo-deposition of Pt as a 0.1 wt.% co-catalyst onto the surface of the materials. The lamp was switched off after ~2 h. Note that mercury light consists of several spikes at different wavelengths and is not a continuous light source, as compared to Xe light (see supporting information (SI) **Figure S1**). The main role of a co-catalyst in photocatalytic water splitting is to extract the photoexcited electrons from the conduction band while providing as active sites for the gas evolution. Pt is known to be a good hydrogen evolution co-catalyst due to its very low overpotential for this reaction. Ethanol, a sacrificial agent, showed an H_2 evolution of only ca. 1/10 of the target materials and is presented as a control test of the activity with respect to the synthesized materials (see **Figure 12**). The control test is performed with the aqueous solution of ethanol in absence of Pt co-catalyst.

3. COMPUTATIONAL

3.1 Bond valence sum and global instability index

In order to evaluate the possible arrangements of O and F in $LaBaInO_3F_2$, bond valence sums (BVSs)[31] and global instability indices (GIIs)[32] were calculated using the atomic positions determined from ADT in combination with the lattice parameters from PXRD.

BVSs and GIIs for systems with partial occupancies, possibly including vacancies, can be calculated according to the following equations. First, the bond valence $s_{ij}^{\alpha\beta}$ between site i occupied by element α and site j occupied by element β is computed as

$$s_{ij}^{\alpha\beta} = \exp\left(\frac{R_0^{\alpha\beta} - r_{ij}}{b}\right), \qquad \text{(Equation 1)}$$

where r_{ij} is the distance between sites i and j, $R_0^{\alpha\beta}$ is an empirical parameter specific for the ionic pair α and β, and b is an empirical parameter independent of the ionic pair. Next, the bond valences of the system are used to calculate site-occupancy-weighted sums S_i^{α} as

$$S_i^{\alpha} = \sum_{\alpha}\sum_{j}\sum_{\beta} x_i^{\alpha} x_j^{\beta} s_{ij}^{\alpha\beta}, \qquad \text{(Equation 2)}$$

where x_i^{α} is the occupancy of element α at site i. The occupancies should satisfy $0 \leq x_i^{\alpha} \leq 1$ and $\sum_{\alpha} x_i^{\alpha} \leq 1$. The BVS of site i is then obtained as a weighted sum according to

$$S_i = \sum_{\alpha} x_i^{\alpha} S_i^{\alpha}, \qquad \text{(Equation 3)}$$

The GII is finally obtained as the root mean square error of the BVSs from the formal valences for all the atoms as

$$\mathrm{GII} = \sqrt{\frac{\sum_i (S_i - V_i)^2}{N}}, \qquad \text{(Equation 4)}$$

where V_i is the site-occupancy-weighted average of the formal valence at site i, and $N = \sum_i \sum_{\alpha} x_i^{\alpha}$ is the number of atoms.

The BVS/GII calculations were performed using our own implementation with properly taking care of partial occupancies as described above (SoftBV (Ver. 1.2)[33] does not properly handle partial occupancies). Based on literature values,[31, 34] we utilized an $R_0^{\alpha\beta}$ of 2.057 Å[34], 2.188 Å,

1.792 Å, 2.172 Å, 2.285 Å and 1.902 Å for La–F, Ba–F, In–F, La–O, Ba–O, and In–O, respectively, while b = 0.37 Å was used for all the ionic pairs. The cut-off distance was set to 6 Å. As detailed below in **section 4.4**, we investigated 13 selected O/F arrangements, and the one with 75 % and 50 % occupation of fluoride ions at the apical and the interstitial sites, respectively, showed the lowest GII.

3.2 *Ab initio* DFT

To analyze the electronic structure of $LaBaInO_4$ and $LaBaInO_3F_2$, we conducted *ab initio* DFT calculations. **Figure 2** shows the investigated atomistic models of $LaBaInO_4$ and $LaBaInO_3F_2$. The optimized structural parameters are tabulated in SI **Table S1**. To approximate the disorder of La/Ba at practical computational costs, these two elements were put alternatingly in the La/Ba planes. To achieve this, the simulation cell of $LaBaInO_4$ was constructed from a $\sqrt{2} \times \sqrt{2}$ expansion of the conventional unit cell shown in **Table 1**. For $LaBaInO_3F_2$, based on the GII analysis (see details in **section 4.4**), we considered the configuration where the fluoride ions occupy 75 % and 50 % of the apical and the interstitial sites, respectively.

The *ab initio* calculations were done based on the projector augmented wave (PAW) method[35] implemented in VASP 6.3.0.[36] The plane-wave cut-off energy was set to 520 eV, and La 5s5p6s4f, Ba 5s5p6s, In 5s5p, O 2s2p, and F 2s2p orbitals were treated as valence states. For the structural optimization, the generalized gradient approximation (GGA) in the Perdew–Burke–Ernzerhof (PBE) form[37] was employed. The Brillouin zones of $LaBaInO_4$ and $LaBaInO_3F_2$ were sampled by Γ-centered 6×6×3 and 3×6×6 k-point meshes, respectively, and Gaussian smearing with a width of 0.1 eV was employed. In each ionic step, total energies were minimized until they converged to within 1×10^{-6} eV per simulation cell. Cell volume, cell shape, and internal atomic positions were optimized so that the forces on atoms and the stress components on the unit cell became less than 1×10^{-2} eV/Å and 1×10^{-4} eV/Å^3,

respectively. The partial densities of states (PDOSs) were then computed using the hybrid functional in the Heyd–Scuseria–Ernzerhof form[38] with the parametrization of Krukau et al. (HSE06).[39] To reduce the computational costs, the PBE-optimized structures were adopted, and reduced k-point meshes of 4×4×2 and 2×4×4 were applied for $LaBaInO_4$ and $LaBaInO_3F_2$, respectively, together with the tetrahedron method with the Blöchl correction.[40] For the projection of the plane waves onto atomic regions, following our previous study,[41] we considered radii that were 0.15 Å larger than those of Shannon,[42] i.e., 1.216 + 0.15 = 1.366 Å for La^{3+} (IX), 1.47 + 0.15 = 1.62 Å for Ba^{2+} (IX), 0.8 + 0.15 = 0.95 Å for In^{3+} (VI), 1.4 + 0.15 = 1.55 Å for O^{2-} (VI), and 1.33 + 0.15 = 1.48 Å for F^- (VI).

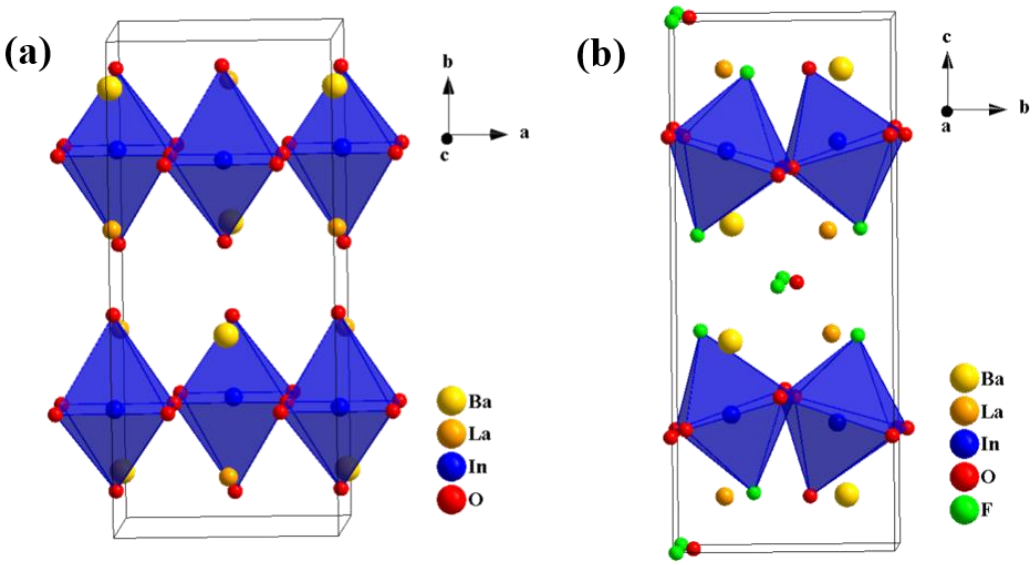

Figure 2 *Atomistic models of $LaBaInO_4$ (a) and $LaBaInO_3F_2$ (b) employed for the ab initio calculations.*

4. RESULTS AND DISCUSSION

4.1 Structural Analysis of $LaBaInO_4$ and its Fluorinated Phase $LaBaInO_3F_2$

PVDF-based methods for the fluorination of oxide materials are known for good stoichiometry transfer; however, it is also known that for substitutive fluorination reactions different phases can be stable, and not every value of x in $A_2BO_{4-x}F_{2x}$ can be achieved.[16] Thus, we examined various ratios of x/n$(CH_2CF_2)_n$ to $LaBaInO_4$. It was found that a two-phase mixture containing

the starting oxide compound plus another phase was formed in the range of $0 < x < 1$ (see SI **Figure S 2**). For $x = 1.05$, we observed the disappearance of the starting oxide phase. Instead, a pattern which is indicative for fluorinated RP-type phases with significant shifts of reflections to smaller angles as well as splitting of some of the reflections (see Error! Reference source not found.) was observed. This pattern could be indexed in the monoclinic crystal system with lattice parameters of $a = 13.6284(3)$ Å, $b = 5.99217(10)$ Å, $c = 5.92016(11)$ Å, and $\beta = 90.886(2)°$ with additional indication for a *C*-centered cell, which is in contrast to the tetragonal symmetry found for the starting material ($a = 4.17797(5)$ Å and $c = 12.97255(19)$ Å; note that also lower symmetries have been reported for $LaBaInO_4$ with a small orthorhombic distortion and the space group *Pbca*, $a = 12.933(3)$ Å, $b = 5.911(1)$ Å, $c = 5.905(1)$ Å[22, 43]). In **Figure 4 (a)**, for $LaBaInO_4$, the reflections appearing at $2\theta = 26.75°$, and 27.21° correspond to K_β of (103) and (110) reflections, respectively. The reflections at $2\theta = 27.44°$ correspond to the allowed reflection (004) of *I4/mmm*. In addition to the oxyfluoride phase, another phase with a broader reflection is observed at 2θ of ~ 28°, which is, according to our experience, indicative for a monoclinic phase with a higher fluoride content with a larger *c* lattice parameter ($c = 16.502(12)$ Å) (see Error! Reference source not found. **(b)**). We would like to emphasize that the detailed structural model of this phase has not been determined. The reflections of the highly fluorinated phase can be well fitted with a symmetry-lowered monoclinic phase, with the atoms located on the pseudo-tetragonal sites and with a fully fluorinated sublattice, e.g., as has been found for fluorinated La_2CoO_4,[13] while only relaxing the lattice parameters to some degree. This additional phase could not be assigned to potential decomposition products such as LaOF, BaF_2, *etc*. We acknowledge that increasing the value of *x* far above 1 resulted in enhanced decomposition of the material (see SI **Figure S 2**). The samples, $LaBaInO_4$ and the related oxyfluoride ($LaBaInO_3F_2$) were prepared various times and are reproducible with minor differences in the lattice parameters of $LaBaInO_4$, $a = (4.17838 \pm 0.00033)$ (Å); $c = (12.9729$

± 0.0024) (Å), and the fractions of the fluorinated phase to the highly fluorinated phase (5.71 ± 1.12) wt% in $LaBaInO_3F_2$. Additionally, Rietveld refinement scans for the angular range, 2θ = 10-130°, of aged samples, $LaBaInO_4$ as well as $LaBaInO_3F_2$, have been provided to the supporting information **Figure S 3**.

ATR-FTIR transmission spectra studies (see SI **Figure S 4**) were performed to further confirm that there is no residue of carbon and unreacted organic polymer left after heating the oxide with PVDF. Furthermore, TGA results show (see SI **Figure S 5**) that the initial weight loss observed below 100 °C in both the cases, $LaBaInO_4$ as well $LaBaInO_3F_2$, is related to surface water adsorption on the sample due to aging at ambient condition. The mass loss approximately 1.5 % was observed at a temperature around 200 °C which might be possible due to water uptake in the aged samples.[44]

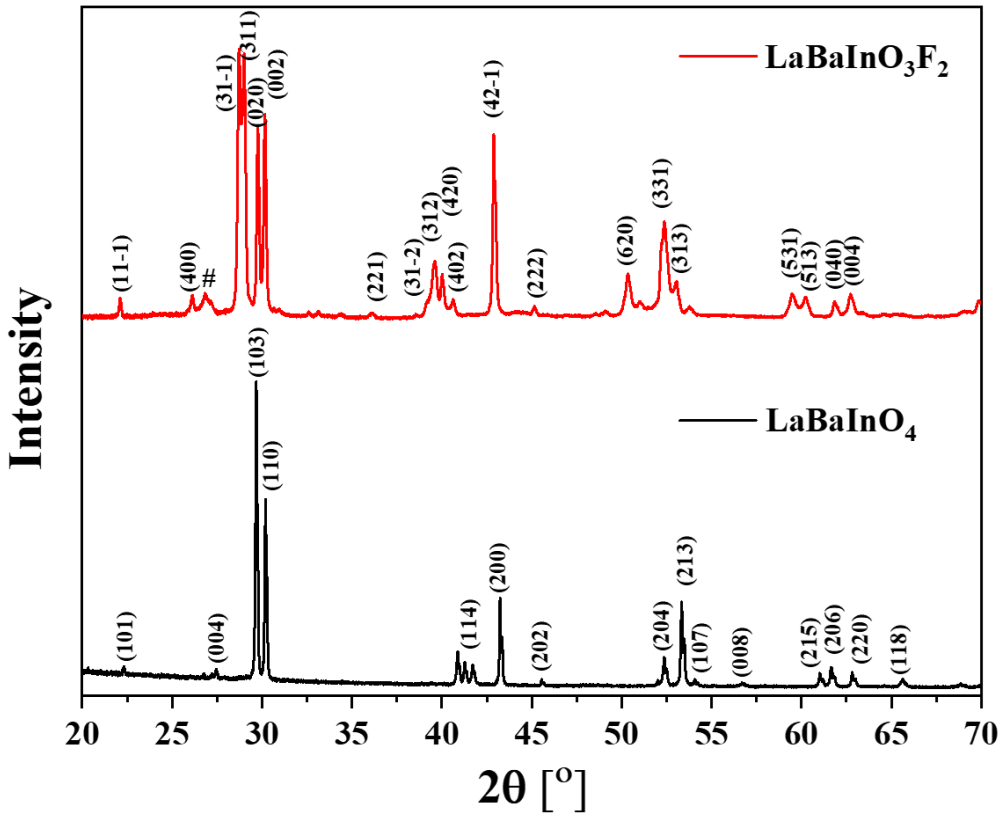

Figure 3 *PXRD patterns of $LaBaInO_4$ and $LaBaInO_3F_2$.*

(#indicates the highly fluorinated phase)

Oxide and fluoride ions are the weakest scatterers within the structural matrix of La/Ba/In, and X-ray diffraction cannot provide sufficient information on the anion sublattice nor any details on the structural distortion. To derive an improved structural model of the monoclinic phase obtained after fluorination, a Fast-Automated Diffraction Tomography (FAST-ADT) measurement was performed. The STEM image and the reflections obtained from the ADT measurement are provided in the supporting file (SI, **Figure S 6**). The reflections obtained for the cell of the main compound are found to be *C*-centered, $h + k = 2n$ (001), and consistent with a monoclinic phase with space group *C*2/*c* (15). The obtained structural parameters with an observed R-value from the dynamical refinement of 10.93 % are shown in **Table 1**. This structural model can be used to obtain an excellent fitting of the intensities observed via PXRD within a Rietveld analysis, see Error! Reference source not found..

Table 1 *Refined structural parameters for $LaBaInO_4$ and $LaBaInO_3F_2$ (from PXRD and ADT). The subscripts "eq", "ap", and "int" indicate the equatorial, the apical, and the interstitial positions, respectively.*

Phase	Atom	Wyckoff site	*x*	*y*	*z*	Occupancy
$LaBaInO_4$ *I*4/*mmm* (139) *a* = 4.17890(5) Å *c* = 12.9732(2) Å *V* = 226.553(6) Å^3	La1	4*e*	0	0	0.35599(5)	0.5
	Ba1	4*e*	0	0	0.35599(5)	0.5
	In1	2*a*	0	0	0	1
	O_{eq}	4*c*	0	1/2	0	1
	O_{ap}	4*e*	0	0	0.17608	1
	R_{wp} = 6.25; R_{Bragg} = 3.571; GOF = 1.12 (PXRD)					
$LaBaInO_3F_2$ *C*2/*c* (15)	La1	8*f*	0.39531	0.75254	0.47969	0.5
	Ba1	8*f*	0.39531	0.75254	0.47969	0.5

a = 13.6284(3) Å b = 5.99950(9) Å c = 5.92374(9) Å β = 90.886(2)° V = 483.2597(3) Å^3	In1	4*d*	1/4	1/4	1/2	1
	$(O/F)_{eq}$	8*f*	0.26974	0.97685	0.72604	1 (in total)
	$(O/F)_{ap}$	8*f*	0.40431	0.34090	0.53177	1 (in total)
	$(O/F)_{int}$	4*e*	1/2	0.97822	3/4	1 (in total)
	$R_{(observed)}$ = 10.93; GOF = 5.84 (ADT)					
	R_{wp} = 7.08; R_{Bragg} = 6.776; GOF = 3.30 (PXRD)					

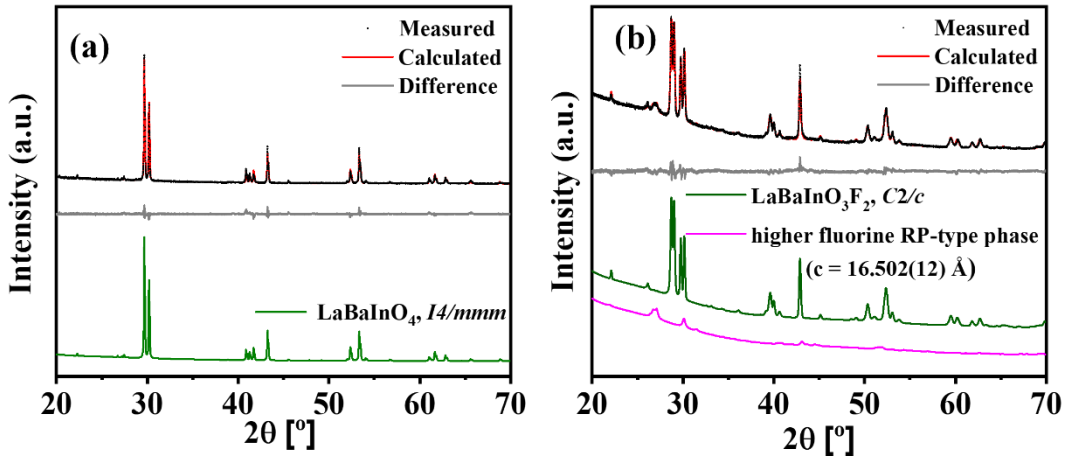

Figure 4 *Rietveld analysis of PXRD data of $LaBaInO_4$ (a) and $LaBaInO_3F_2$ (b).*

The obtained structural model is similar to what was found for $La_2NiO_3F_2$[45] and its slightly reduced phase $La_2NiO_3F_{1.93}$,[46] reported previously by our group. The similarity arises from the observation that only half of the interstitial anion sites are filled in an ordered way, which can be considered as the main origin for the structural distortion. This implies an overall composition of $LaBaInX_5$ (X = O/F). From the fact that In is quite stable in its trivalent oxidation state, as confirmed by XPS and XAS analysis (see **section 4.3**), and from the consistency of the structure with the amount of fluorination agent used, we conclude that the new monoclinic phase has a composition close to $LaBaInO_3F_2$.

To evaluate possible anion ordering scenarios, the BVSs and the GIIs were evaluated for 13 selected O/F occupation patterns in $LaBaInO_3F_2$ based on the atomic positions determined from ADT in combination with the lattice parameters from PXRD. **Table S2** (see SI) shows the thus obtained GIIs in ascending order. Among the considered arrangements, the lowest GII is found for the configuration with 75 % and 50 % of fluoride ions at the apical and the interstitial sites, respectively, which may thus be thermodynamically preferable. This is in contrast to $La_2NiO_3F_2$,[45] where the fluoride ions are located mainly at the apical anion sites. The highest GII is found for the configuration with full F occupation at the equatorial sites, which is therefore unlikely to occur. **Figure 5** shows the crystal structure of $LaBaInO_3F_2$ obtained by the combination of PXRD and ADT with the just-discussed anion ordering.

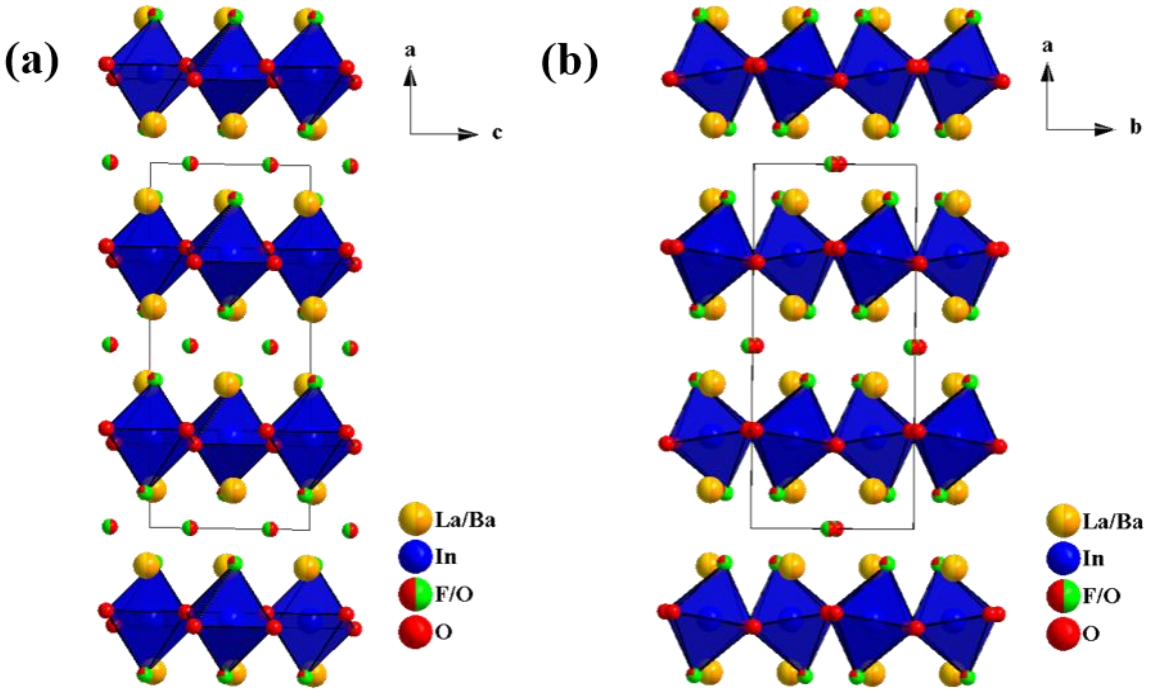

Figure 5 *Crystal structure of $LaBaInO_3F_2$ with an occupation of anions at the equatorial (O_{eq}), apical ($(O/F)_{ap}$) and interstitial ($(O/F)_{int}$) sites with oxygen and fluoride in a 1:0, 0.25:0.75 and 0.5:0.5 ratio, respectively, with viewing directions along the b-axis (a), and the c-axis (b).*

In comparison to the parent oxide $LaBaInO_4$, $LaBaInO_3F_2$ shows significant changes in bond distances, which mainly originates from a tilting of the octahedra within the

$In((O/F)_{eq})_4((O/F)_{ap})_2$ subnetwork (see **Table 2**). First, the La/Ba ions show a change of coordination environment due to the half filling of the interstitial sites. For the indium ions, a strong decrease of the bond distance to the apical ions by ~ 0.11 Å can be observed, which is considerably higher than the difference of ionic radii of oxide and fluoride ions (Δ ~ 0.07 Å). For the fluorinated phase $LaBaInO_3F_2$, the anions on the interstitial sites possess the shortest distance to La/Ba ions in the order of 2.52–2.56 Å. At the same time, the anions on the equatorial sites move further away from the indium ions by 0.04–0.05 Å, which appears to be facilitated by the strong shortening of the bond of the equatorial anion to one of the La/Ba ions (from 2.83 Å to 2.63 Å). Therefore, the substitution and filling of the interstitial sites is accompanied with changes of the bond distances and polyhedra in such a way that the charge neutrality along the La/Ba/In remains well balanced locally.

Further, it is of interest to compare the structure of $LaBaInO_3F_2$ to related oxide and oxyfluoride compounds. The difference of the two in-plane axes in $LaBaInO_3F_2$ is quite low (5.99 Å – 5.92 Å = 0.07 Å), and thus much lower than what has been observed for $La_2NiO_3F_2$ (5.79 Å – 5.49 Å = 0.30 Å), regardless of the similarity in tilting of the octahedra. This can be explained by the larger ionic radii[42] of Ba^{2+} than La^{3+} and In^{3+}, which increase the in-plane space requirements, resulting in a significant increase of the long crystallographic axis (+0.62 Å for $LaBaInO_4 \rightarrow LaBaInO_3F_2$ as compared to +0.17 Å for $La_2NiO_4 \rightarrow La_2NiO_3F_2$[45]). Similar behavior was also observed recently by Jacobs et al.[47] for the $La_2NiO_4 \rightarrow La_2NiO_3F_2 \rightarrow La2NiO_{2.5}F_3$ series, where the Ni-F_{ap} distance decreases with increasing interstitial anion occupation.

$LaBaInO_3F_2$ is not the only RP-type indium-based oxyfluoride known: Ba_2InO_3F, a member of the series Ba_2InO_3X (X = F, Cl, Br) was reported in the literature[48] and can be synthesized by high-temperature sintering of precursor salts of halides, oxides, and carbonates. The phase crystallizes in the tetragonal space group *P4/nmm* and a full ordering of oxide and fluoride ions

on the apical sites was found, which results in the existence of Ba-F and Ba-O layers originating from the locally polar octahedral coordination environments $In((O/F)_{eq})_4((O/F)_{ap})_2$. The partial structure of the perovskite blocks in the $LaBaInO_3F_2$ crystal framework represents a tilting of $a^+b^-b^-$ in the Glazer notation, resulting in a monoclinic structure with the space group of *C*2/*c* (see SI **Figure S 7**).

Table 2 *Refined bond distances of $LaBaInO_4$ and $LaBaInO_3F_2$ (C2/c, 15).*

Bond	**Bond length (Å)**	
	$LaBaInO_4$	**$LaBaInO_3F_2$**
(La/Ba)1–$(O/F)_{eq}$	2.829(2) (4x)	2.633(5) (1x) 2.780(5) (1x) 2.889(1) (1x) 3.307(9) (1x)
(La/Ba)1–$(O/F)_{ap}$	2.293(6) (1x) 2.978(1) (4x)	2.487(7) (1x) 2.714(7) (1x) 2.789(4) (1x) 3.316(3) (1x)
(La/Ba)1–$(O/F)_{int}$	--	2.520(5) (1x) 2.558(4) (1x)
In1–$(O/F)_{eq}$	2.089(1) (4x)	2.130(6) (2x) 2.138(2) (2x)
In1–$(O/F)_{ap}$	2.284(1) (2x)	2.177(6) (2x)

4.2 Analysis of Chemical States via Spectroscopic Methods

XPS has been performed to study the elements present on the surface and their oxidation states. The comparative XPS spectra of the oxide $LaBaInO_4$ and oxyfluoride $LaBaInO_3F_2$ are shown in Error! Reference source not found.. In the 3d XPS spectra show a shift on the order of 0.2–0.3 eV to lower binding energies. Since the topochemical fluorination of $LaBaInO_4$ to $LaBaInO_3F_2$ is achieved via a non-oxidative substitutive chemical reaction where one O^{2-} anion is substituted by two F^- anions (conducting the reaction in air lowers the reductive power of the polymer),[16] the oxidation state of indium (In^{3+}) in the octahedra should not change upon fluorination. The shift in XPS should therefore be not attributed to a chemical shift due to a change of the oxidation state but rather to the changes of cation–anion distances due to the substitution of O^{2-} anions with F^- anions. The elemental spectra of F 1s confirm the presence of fluorine atoms in $LaBaInO_3F_2$ (**Figure 6**). For $LaBaInO_4$, the main peak of the O 1s spectrum at 531.0 eV arises from lattice oxygen and is typical for similar perovskite systems.[49] For $LaBaInO_3F_2$, the O 1s spectrum also confirms the presence of interstitial O^{2-} anions, which can be seen as a shoulder towards lower binding energies. Such lower binding energies can be expected due to the absence of bonding to the In^{3+} ions, which would result in stronger covalent bonds. In addition to this absence, the disorder of La/Ba and O/F also further influences the shape of the O 1s peak in $LaBaInO_3F_2$. Particularly, the O 1s peak shows a shoulder around 528 eV. This may originate from the O^{2-} ions at the interstitial sites, which should have lower binding energies than those at the equatorial or the apical sites. Further analyses of the Ba and La spectra reveal the absence of additional peaks, meaning that there is no indication of the formation of side products at the surface. La, Ba, and In have precise oxidation states (no mixed valency as could be found in Ni/Co/Cu-RP-type compounds [45, 50]), and hence one can assign an anion content close to $LaBaInO_3F_2$ to this compound.

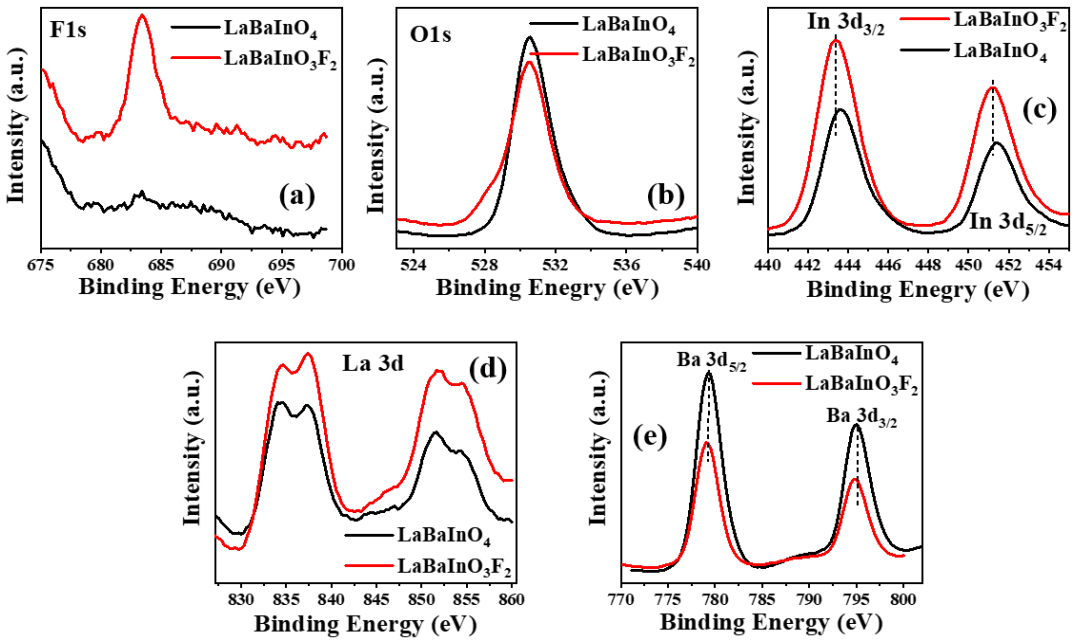

Figure 6 *Comparative XPS spectra of $LaBaInO_4$ and $LaBaInO_3F_2$: (a) F 1s, (b) O 1s, (c) In 3d, (d) La 3d, and (e) Ba 3d*

X-ray absorption spectroscopy has been done to understand the local electronic environment around indium inside the bulk. The XAS spectra for the L_3-edge of indium in $LaBaInO_4$ and $LaBaInO_3F_2$ are presented in Error! Reference source not found.. The spectra of the oxide and the oxyfluoride are mostly in agreement at the absorption edge and only show a small shift of the first peak around 3.73 keV to lower energies by about half an eV upon fluorination, consistent with the observation in XPS. Thus, we conclude that the bulk and surface of the material behave similarly, and that both compounds show the same +3 oxidation state for indium. In agreement with the structural changes, all changes in peak intensities can be understood in terms of a competition between the bond distances within the perovskite layers and the interstitial anions, and the resulting interplay among the O 2p, F 2p, and In 3d orbitals.

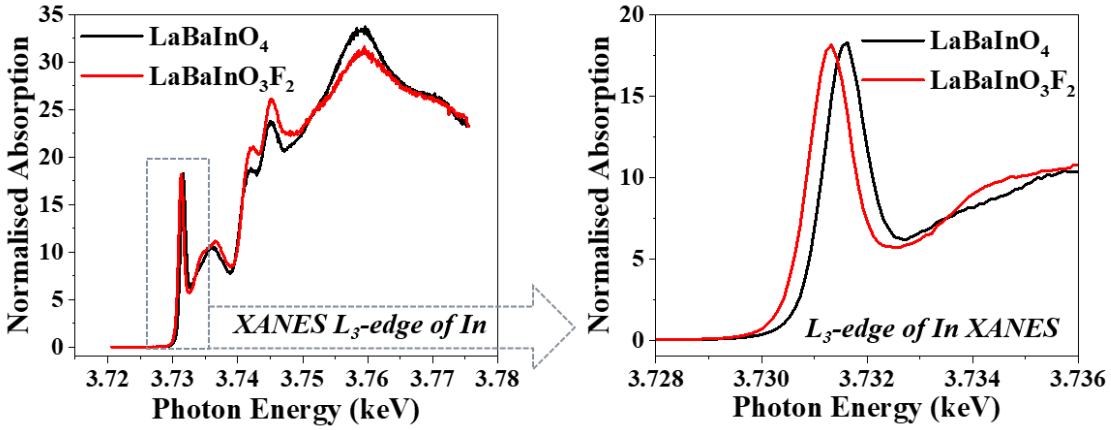

Figure 7 *L_3-edge XAS absorption of indium in $LaBaInO_4$ and $LaBaInO_3F_2$.*

4.3 Optical Properties

To understand the recombination of photoexcited electrons and holes, steady-state room temperature photoluminescence (RT-PL) measurements have been performed for a broad range of excitation wavelengths. The results are presented in **Figure 8**. The comparison of the emission spectra shows a clearly different emission behavior of $LaBaInO_4$ compared to $LaBaInO_3F_2$. In $LaBaInO_4$, one main emission band centered at about 2.3 eV (540 nm) is observed regardless of the excitation wavelength (**Figure 8 (a)**). This emission band likely corresponds to direct band transitions (conduction band to valence band) leading to radiative recombination. For the fluorinated compound $LaBaInO_3F_2$ (**Figure 8 (b)**), in contrast, two emission bands centered at about 2.7 eV (460 nm) and 3.5 eV (350 nm) can be seen. When the fluorinated compound is excited with the lower wavelength of 280 nm, it produces a strong emission spectrum at 2.7 eV and a weaker emission spectrum at 3.5 eV (about half of the intensity found at 2.7 eV). The weaker spectrum at 3.5 eV becomes increasingly more pronounced when the excitation wavelength is increased (excitation energy is lowered). Thus, excitation with a wavelength of 290 nm results in two pronounced emission spectra, one at the higher energy of 3.5 eV and the other at the lower energy of 2.7 eV. When excited with further increased wavelengths of 300–320 nm, the emission band at 3.5 eV becomes very dominant,

while the emission band at 2.7 eV is seen only as a weak shoulder. The PL emission spectra has been also measured at longer wavelength excitations ranging from 400–500 nm (see SI **Figure S 8**) which show further absorption at lower energy.

Based on the PL spectra, the fluorinated compound might have an indication for an indirect gap (emission energy of 2.7 eV) inside of its fundamental, direct bandgap (emission energy of 3.5 eV). The emission energy of 2.7 eV corresponding to the indirect band gap is possibly caused by delayed or non-radiative recombination in the form of heat. They might be induced by the presence of the interstitial anions in the rock salt type layers and should help to mobilize photoexcited carriers. The mobile carriers can lead to delayed radiative recombination and hence delayed emission, which is also supported by comparing the intensity counts of the oxide and oxyfluoride compound. For $LaBaInO_3F_2$, the counts are decreased by a factor of 100 compared to $LaBaInO_4$, as shown in **Figure 8**. There is a strong correlation between the PL emission intensity which results from the radiative recombination of free charge carriers and the lifetime of the photoexcited e^-–h^+ pairs.[51] A reduction in emission intensity can be attributed to an enhanced carrier lifetime, suggesting that the fluorination leads to longer-lived charge carriers. Furthermore, fluoride ions are capable of trapping photogenerated electrons and promote the separation of e^-–h^+ pairs, since fluorine is the most electronegative element thereby possessing a strong electron withdrawing ability which can reduce the recombination of the photogenerated carriers.[52]

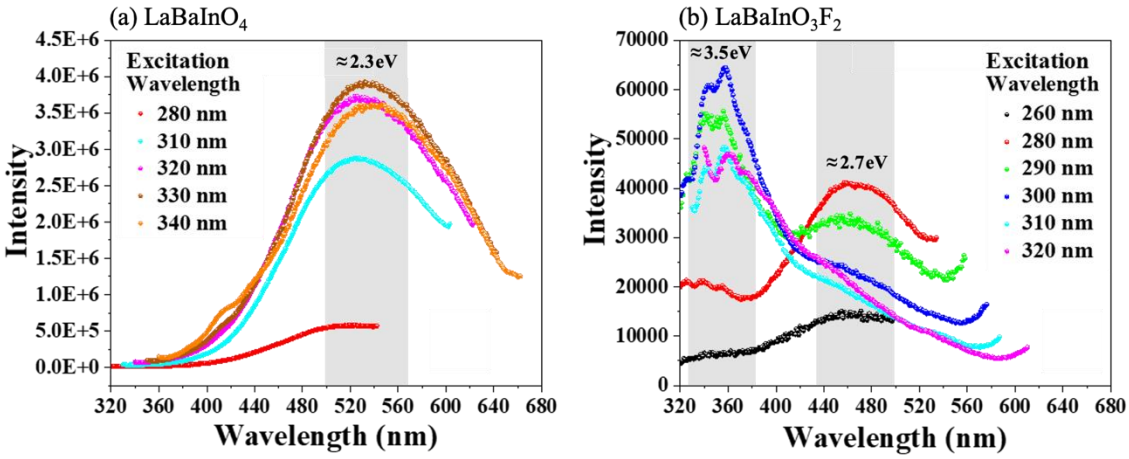

Figure 8 *RT-PL emission spectra of (a) $LaBaInO_4$ and (b) $LaBaInO_3F_2$ at different excitation wavelengths as given in the legend. The shaded regions indicate emission bands with the energy values reflecting the center of the region.*

The UV-Vis DRS spectra shown in **Figure 9** (see SI **Figure S 9** for absorbance vs. wavelength) support the observation from the PL spectra. There is one main absorption edge for the oxide material at about 1.8 eV, which can be matched with the single emission band observed in the PL measurement (centered at about 2.3 eV). For the oxyfluoride, two absorption edges at about 1.9 eV and 3.3 eV are seen in the DRS spectra, which is likewise consistent with the two emission bands in the PL spectra of the fluorinated compound. As for the type of the bandgap, its determination from DRS measurements is in general difficult. However, the lower-energy absorption edge in the oxyfluoride seems to originate from indirect transitions based on its relatively small slope as compared to the higher-energy absorption edge. Such an interpretation is indeed consistent with the PL intensity alluded to above. Overall, the results from the optical measurements reveal a significant impact of the fluorination on the optical behavior. Further, they confirm the potential of the present compounds to absorb light in the UV to the visible region, making both materials potential candidates to harvest solar energy. $LaBaInO_4$ appears dark brown to the eye, whereas $LaBaInO_3F_2$ powders possess a dull hue white represented in the supporting information (see SI, insets of **Figure S 9**). In a recent study, Jacobs et al.[47] reported on the oxyfluoride system prepared by topochemical low-temperature fluorination of

La_2NiO_4 with PVDF to $La_2NiO_3F_2$ and $La_2NiO_{2.5}F_3$, which show a strong bandgap increase compared to La_2NiO_4 (3.2 eV, 3.4 eV vs 1.3 eV, respectively).

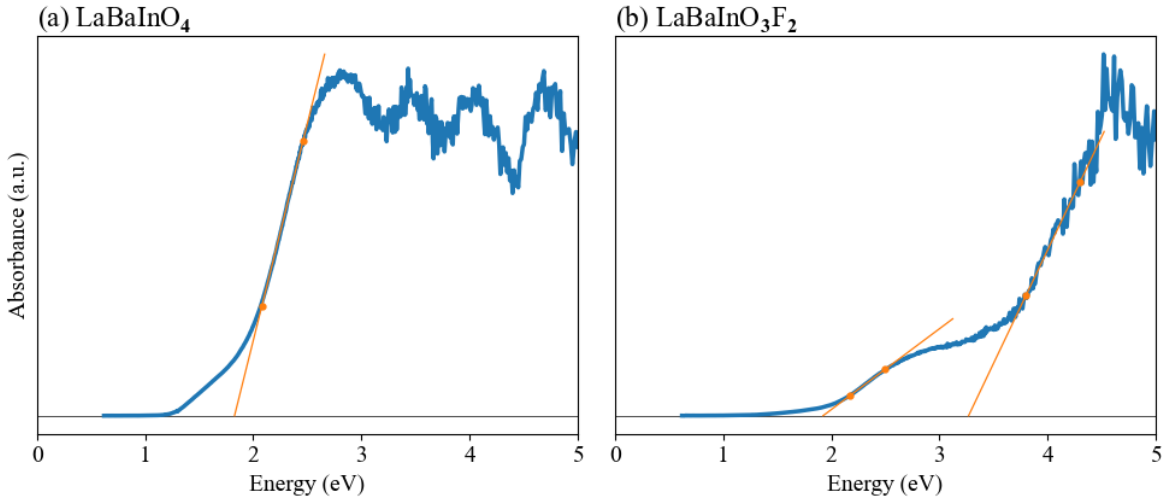

Figure 9 *UV-Vis DRS absorbance spectra of (a) $LaBaInO_4$ and (b) $LaBaInO_3F_2$. The regions used for the linear fits to estimate the bandgaps are indicated by the orange, filled circles.*

4.4 Optical Properties *via* DFT Calculations

To better understand the electronic structure of both $LaBaInO_4$ and $LaBaInO_3F_2$, we conducted *ab initio* DFT simulations based on the HSE06 hybrid functional. **Figure 10** shows the thus obtained PDOSs per ion. Note that the PDOSs for the cations are much lower than those of the anions near the valence-band maxima (VBMa), since the cations provide their valence electrons to the anions. Therefore, to make all PDOSs similarly visible, we rescaled the PDOSs of the cations by 15. For $LaBaInO_3F_2$, based on the GII analysis (SI **Table S2**), we considered the configuration with 75 % and 50 % of the apical and the interstitial sites occupied by fluoride ions.

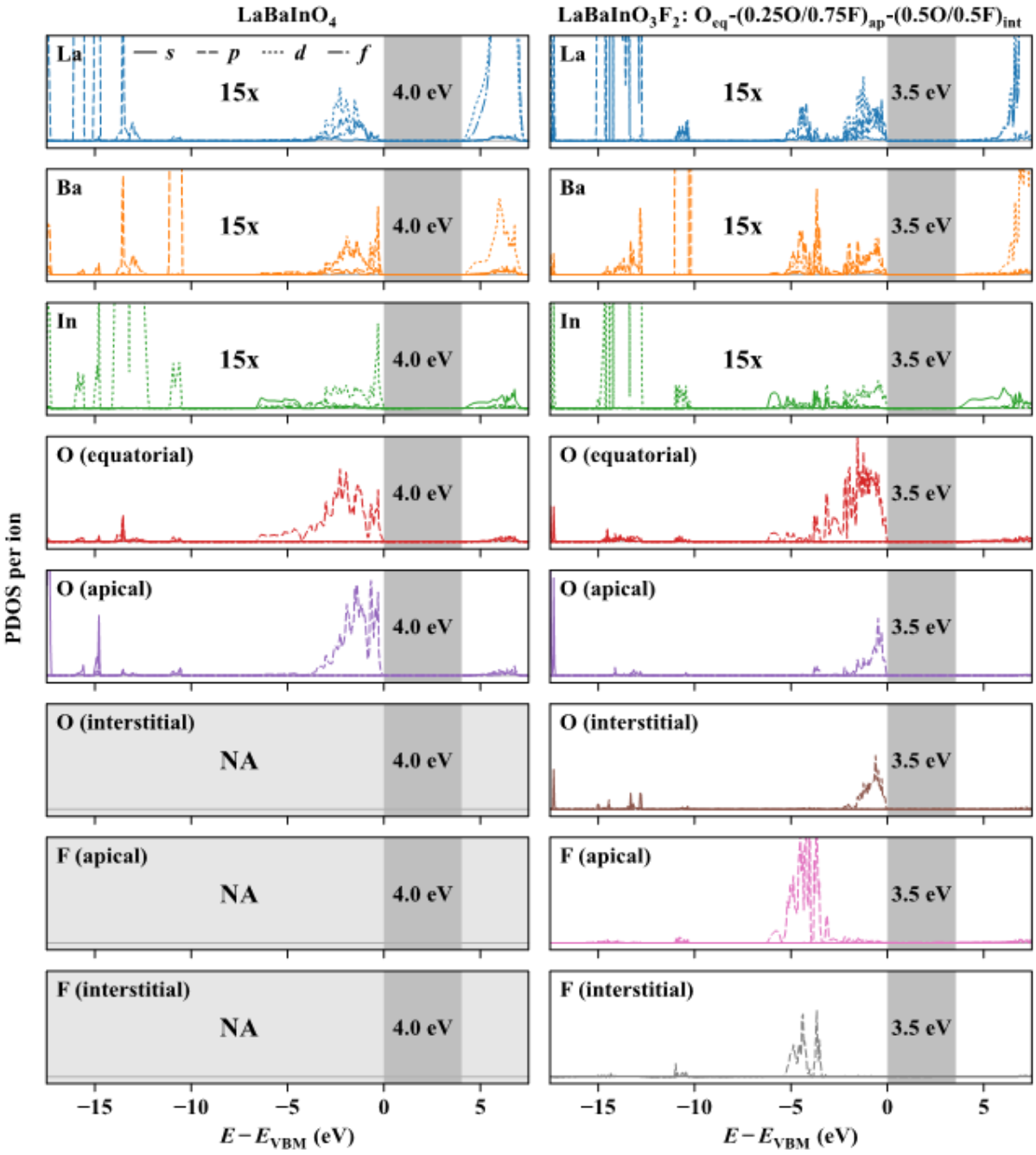

Figure 10 *PDOSs per ion obtained from ab initio DFT calculations with the HSE06 hybrid functional. The valence-band maxima (VBMa) are set as the reference, and the PDOSs of the cations are scaled by a factor of 15 to make them visible.*

For both the oxide and the oxyfluoride, the PDOSs just below the VBMa are made mostly of the 2p electrons of the oxide ions. The PDOS peaks for the fluoride ions in $LaBaInO_3F_2$ are, in contrast, found 4 eV to 5 eV below the VBMa, regardless of which sites they occupy. The fluoride ions hence do not contribute to the VBMa at least directly. For the conduction bands, in $LaBaInO_4$, all of the La 4f5d, Ba 5d, and In 5s orbitals contribute to the conduction-band

minima (CBMa), while in $LaBaInO_3F_2$, the 5s orbitals of In mostly contribute to the CBMa. The obtained band gap is 4.0 eV in the oxide, while after fluorination it reduces to 3.5 eV. This may be partly because of the narrowing of the energy bands for the oxide ions at the apical and the interstitial sites just below the VBMa and possibly due to the broadening of the energy band made of In 5s orbitals just above the CBMa. Due to the disorder of La/Ba and O/F, it is not straightforward to evaluate whether the band gaps are direct or indirect solely from the DFT results. The larger band gaps obtained from the calculations as compared to the experimental DRS results may be caused by finite size effects in the calculations. Specifically, larger model systems may be required to better capture the chemical disorder.

4.5 Morphological Properties and Photocatalytic Hydrogen Evolution

The fluorination reaction is a topochemical reaction performed at low temperatures. This can be considered favorable for comparing chemically modified compounds in terms of surface-sensitive properties such as photocatalytic activity, since surface morphologies should not change significantly. To examine the morphology, SEM images were recorded and are shown in **Figure 11** for $LaBaInO_4$ and $LaBaInO_3F_2$. For both compounds, the grains are irregular, round-shaped particles, and the average grain size is in the micrometer range as typically obtained from solid-state synthesis. The grain surfaces are clean without indication of additional phases. No morphological changes were observed upon fluorination. Thus, we conclude that both powders can be used to investigate and compare the intrinsic chemical influence on photocatalytic properties.

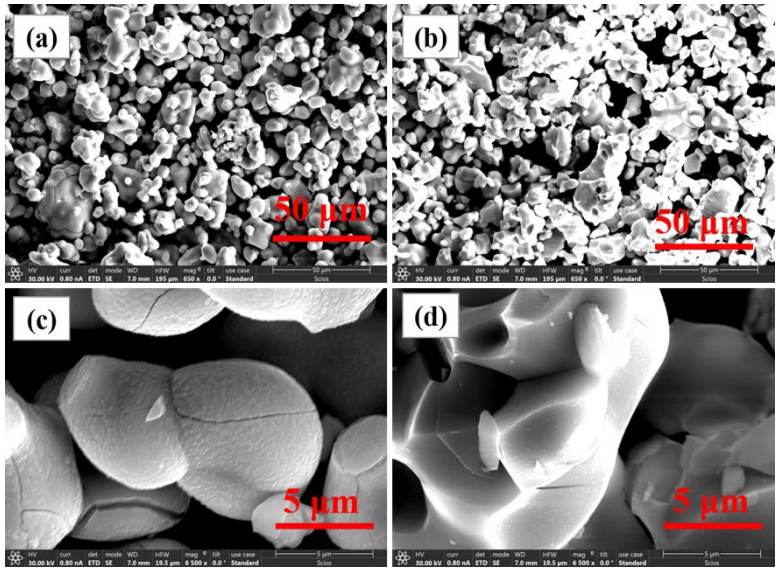

Figure 11 *SEM images at two different magnifications of 650x (50µm) and 6500x (5µm). (a and c) $LaBaInO_4$. (b and d) $LaBaInO_3F_2$.*

Photocatalytic hydrogen evolution experiments were performed on the oxide $LaBaInO_4$ and oxyfluoride $LaBaInO_3F_2$, in presence of the co-catalyst Pt (0.1 wt.%), to observe the photocatalytic activities of both the compounds. The obtained results are presented in **Figure 12** showing that both materials are photocatalytically active for sacrificial H_2 evolution, with similar H_2 evolution rates. The decline of the H_2 evolution rate observed in **Figure 12** after 2 h shows that there is no hydrogen evolution in the absence of light. Moreover, the H_2 evolution rates of the samples surpass by far the H_2 evolution of the sacrificial agent—that is without any photocatalytically active sample—showing that the vast majority of the evolved H_2 stems from photocatalysis on the oxide/oxyfluoride samples.

It is worthwhile to stress that, for the fluorinated compound, despite the substantial changes in the optical properties, the energy remains in the required range suitable for photocatalytic water-splitting, and the hydrogen evolution rate stays nearly unaffected. This might be an indication of better charge separation in the fluorinated samples.[52, 53] However, further studies are needed to understand this aspect in detail. Similarity of the activity between the oxide and the oxyfluoride is surprising with respect to the altered optical properties upon fluorination,

especially since an additional influence of surface wettability has been previously reported by Kuriki and co-workers for $Pb_2Ti_2O_{5.4}F_{1.2}$.[54] The structural impact upon fluorination opens possibilities for modification of RP-type structures to improve the chemical and optical properties—and thereby the functional properties—without modifying the morphology. Further studies to improve the morphology and microstructural architecture are necessary by preparing materials with higher surface areas.[55]

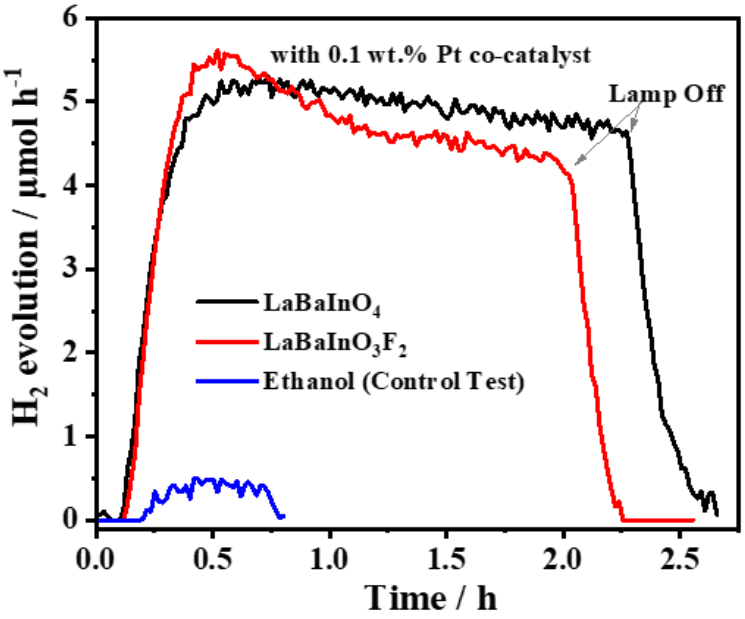

Figure 12 *Photocatalytic activity for $LaBaInO_4$ and $LaBaInO_3F_2$ in sacrificial hydrogen evolution with 0.1 wt% Pt as co-catalyst under UV light illumination.*

5. CONCLUSIONS

We have shown that the fluorination of RP-type $LaBaInO_4$ to $LaBaInO_3F_2$ is possible at low temperature via a topochemical route. The fluoride incorporation leads to symmetry lowering. The fluorinated phase shows a strong expansion of the lattice along the stacking direction of the perovskite layers, and a channel-like ordering of anions on the interlayer sites with disorder of oxide and fluoride anions on the apical and the interstitial sites. The structural modification has an impact on the optical properties and the color of the materials and thus on the band gap.

PDOSs obtained from *ab initio* DFT simulations also confirm that the band gap is changed after fluorination, which originates from the modified contribution of ions to the VBM and the CBM. In addition, defect states in the oxide and oxyfluoride material are likely to have additional influence on the optical properties. The observed photocatalytic activities for the oxide $LaBaInO_4$ and the oxyfluoride $LaBaInO_3F_2$ are similar regardless of the induced optical changes, with a similar activity for hydrogen evolution. The structural impact suggested here provides a novel approach for altering the chemistry and thus fine tuning of the functionality of layered oxides, without modification of their microstructure. In future, the influence of fluorination chemistry on materials parameters which correlate with the photocatalytic activity, such as changes of the band gap, number of defect states, the impact on the lifetime of charge carriers as well as hydrophilicity / -phobicity[54] of the surfaces of the materials, need to be further understood in order to exploit fluorination chemistry for improving functional properties.

■ AUTHOR INFORMATION

Corresponding Author

*[a]Shama Perween; shama.perween@imw.uni-stuttgart.de +4971168561937, Institute for Materials Science, Chemical Material Synthesis, University of Stuttgart, Heisenbergstrasse 3, 70569 Stuttgart, Germany.

[b]Institute for Materials Science, Technical University of Darmstadt, Alarich-Weiss-Straße 2, 64287 Darmstadt, Germany.

ORCID Id: 0000-0001-9631-5995

Notes

- The authors declare no competing financial interest.

- The first version of the present work in an unformatted pre-print is submitted to the ChemRxiv (Cambridge Open Engage).[56]

■ SUPPORTING INFORMATION

- Additional supporting figures of the measured lamp source spectra, PXRD patterns of $LaBaInO_{4-x}F_{2x}$ with different equivalents of PVDF, Rietveld analysis of PXRD data of aged samples, comparative ATR-FTIR transmission spectra, TGA curves, 3D reciprocal space reconstructed from ADT acquisition, RT-PL emission spectra, and ultraviolet–visible diffused reflectance spectra. The supporting tables of refined structural parameters from *ab initio* DFT calculations as well as bond valence sums (BVSs)/GIIs with the refined structural parameters from XRD and ADT (Table 1) in 13 different O/F arrangements. (**PDF**)
- CCDC/CDS **2289053** contains the supplementary crystallographic data for $LaBaInO_3F_2$.

■ ACKNOWLEDGMENT

S.P. acknowledges funding by the Future Talents Postdoc program and a Career Bridging Grant of TU Darmstadt. S.P. also acknowledges Prof. Dr. Oliver Clemens, (Head of Department, Institute for Materials Science, Chemical Material Synthesis, University of Stuttgart) for providing the research infrastructure and for the valuable scientific discussion. Y.I. and B.G. acknowledge the funding from the European Research Council (ERC) under the European Union's Horizon 2020 research and innovation programme (grant agreement No. 865855), the support by the Stuttgart Center for Simulation Science (SimTech), and the support by the state of Baden-Württemberg through bwHPC and the German Research Foundation (DFG) through grant no INST 40/467-1 FUGG (JUSTUS cluster). S.V. and P.G. acknowledge EcoX (ANR grant number 10-EQPX-0027) for the XAS measurements by using TEXS[29] spectrometer. S.P.

acknowledges Mertcan Han for the ATR-FTIR spectroscopic measurements (Physical Intelligence, Max-Planck Institute, Stuttgart).

■ AUTHOR CONTRIBUTIONS

S.P. developed the idea, synthesized the materials, carried out the majority of measurements, analyzed the data and wrote the manuscript. K.W. helped in BVS calculations. Z.D. and U.K. performed the ADT characterization and provided the calculated data. M.W. and R.M. performed the photocatalytic evaluation for H_2 generation. Y.I. and B.G. performed the DFT calculations and revised the BVS calculations as well as wrote the DFT part in the manuscript. S.V. and P.G. performed the XAS measurements. S.S. measured the UV-Vis DRS. S.P. acknowledges the instrument facilities used such as XPS, TGA, ATR-FTIR at Max Planck Institute for Intelligent Systems, Stuttgart. P.S. performed the XPS measurements, and P.M.J. performed the thermogravimetric analysis (TGA) measurements.

■ REFERENCES

(1) Kalair, A.; Abas, N.; Saleem, M. S.; Kalair, A. R.; Khan, N. Role of energy storage systems in energy transition from fossil fuels to renewables. *Energy Storage* **2020**, *3* (1). DOI: 10.1002/est2.135.

(2) Prier, C. K.; Rankic, D. A.; MacMillan, D. W. Visible light photoredox catalysis with transition metal complexes: applications in organic synthesis. *Chemical Reviews* **2013**, *113* (7), 5322-5363. DOI: 10.1021/cr300503r. Ischay, M. A.; Anzovino, M. E.; Du, J.; Yoon, T. P. Efficient Visible Light Photocatalysis of [2+2] Enone Cycloadditions. *Journal of American Chemical Society* **2008**, *130*, 12886-12887. Asahi, R.; Morikawa, T.; Irie, H.; Ohwaki, T. Nitrogen-doped titanium dioxide as visible-light-sensitive photocatalyst: designs, developments, and prospects. *Chem Rev* **2014**, *114* (19), 9824-9852. DOI: 10.1021/cr5000738. Douglas, J. J.; Sevrin, M. J.; Stephenson, C. R. J. Visible Light Photocatalysis: Applications

and New Disconnections in the Synthesis of Pharmaceutical Agents. *Organic Process Research & Development* **2016**, *20* (7), 1134-1147. DOI: 10.1021/acs.oprd.6b00125.

(3) Kudo, A.; Miseki, Y. Heterogeneous photocatalyst materials for water splitting. *Chem Soc Rev* **2009**, *38* (1), 253-278. DOI: 10.1039/b800489g.

(4) Ansari;, S. A.; Khan;, M. M.; Ansaric;, M. O.; Cho, M. H. Nitrogen-doped titanium dioxide (N-doped TiO_2) for visible light photocatalysis. *New Journal of Chemistry* **2016**, *40*, 3000-3009. DOI: 10.1039/c5nj03478g. Ansari, S. A. Elemental semiconductor red phosphorus/ZnO nanohybrids as high performance photocatalysts. *Ceramics International* **2023**, *49* (11), 17746-17752. DOI: 10.1016/j.ceramint.2023.02.140. Jones;, B. M. F.; Mamba;, G.; Ansari;, S. A.; Maruthamani;, c. D.; Muthuraj;, V.; Nkambule, T. T. I. Simple fabrication and unprecedented visible light response of $NiNb_2O_6$/RGO heterojunctions for the degradation of emerging pollutants in water. *New Journal of Chemistry* **2021**, *45*, 22697–22713. DOI: 10.1039/d1nj04693d. Ansari;, S. A.; Yadav;, H.; Adeel;, M.; Yoo;, K.; Lee, J. J. Solvothermal growth of 3D flower-like CoS@FTO as high-performance counter electrode for dye-sensitized solar cell. *Journal of Materials Science: Materials in Electronics* **2019**, *30*, 6929–6935. DOI: 10.1007/s10854-019-01008-6. Ansari;, S. A.; Cho, M. H. Simple and Large Scale Construction of MoS_2-gC_3N_4 Heterostructures Using Mechanochemistry for High Performance Electrochemical Supercapacitor and Visible Light Photocatalytic Applications. *Scientific Reports* **2017**, *7*, 43055. DOI: 10.1038/srep43055. Ansari;, S. A.; Ansari;, S. G.; Foaud;, H.; Cho, M. H. Facile and sustainable synthesis of carbon-doped ZnO nanostructures towards the superior visible light photocatalytic performance. *New Journal of Chemistry* **2017**, *41*, 9314-9320. DOI: 10.1039/c6nj04070e.

(5) Kisch, H. *Semiconductor Photocatalysis Principles and Applications*; Wiley-VCH Verlag Gmbh & Co. KGaA, 2015.

(6) Asahi, R.; Morikawa, T.; Ohwaki, T.; Aoki, K.; Taga, Y. Visible-light photocatalysis in nitrogen-doped titanium oxides. *Science* **2001**, *293* (5528), 269-271. DOI: 10.1126/science.1061051. Ibhadon, A. O.; Fitzpatrick, P. Heterogeneous Photocatalysis: Recent Advances and Applications. *Catalysts* **2013**, *3* (1), 189-218. DOI: 10.3390/catal3010189.

(7) Zhang, H.; Ni, S.; Mi, Y. L.; Xu, X. X. Ruddlesden-Popper compound Sr_2TiO_4 co-doped with La and Fe for efficient photocatalytic hydrogen production. *Journal of Catalysis* **2018**, *359*, 112-121. DOI: 10.1016/j.jcat.2017.12.031.

(8) Xiao, H.; Liu, P.; Wang, W.; Ran, R.; Zhou, W.; Shao, Z. Ruddlesden–Popper Perovskite Oxides for Photocatalysis-Based Water Splitting and Wastewater Treatment. *Energy & Fuels* **2020**, *34* (8), 9208-9221. DOI: 10.1021/acs.energyfuels.0c02301.

(9) Shimizu, K.-i.; Tsuji, Y.; Hatamachi, T.; Toda, K.; Kodama, T.; Sato, M.; Kitayama, Y. Photocatalytic water splitting on hydrated layered perovskite tantalate $A_2SrTa_2O_7$. nH_2O (A = H, K, and Rb). *Physical Chemistry Chemical Physics* **2004**, *6*, 106 104–101 069. DOI: 10.1039/B312620J.

(10) Beznosikov, B. V.; Aleksandrov, K. S. Perovskite-Like Crystals of the Ruddlesden–Popper Series. *Crystallography Reports* **2000**, *45* (5), 864–870. DOI: 10.1134/1.1312923. Ruddlesden, S. N.; Popper, P. New compounds of the K_2NiF_4 type. *Acta Crystallographica* **1957**, *10*, 538. DOI: 10.1107/S0365110X57001929.

(11) Nowroozi, M. A.; Wissel, K.; Rohrer, J.; Munnangi, A. R.; Clemens, O. $LaSrMnO_4$: Reversible Electrochemical Intercalation of Fluoride Ions in the Context of Fluoride Ion Batteries. *Chem Mater* **2017**, *29* (8), 3441-3453. DOI: 10.1021/acs.chemmater.6b05075.

(12) Kendall, K. R.; Navas, C.; Thomas, J. K.; zurLoye, H. C. Recent Developments in Oxide Ion Conductors: Aurivillius Phases. *Chemistry of Materials* **1996**, *8*, 642-649. DOI: 10.1021/cm9503083.

(13) Nowroozi, M. A.; Ivlev, S.; Rohrer, J.; Clemens, O. La_2CoO_4: a new intercalation based cathode material for fluoride ion batteries with improved cycling stability. *Journal of Materials Chemistry A* **2018**, *6* (11), 4658-4669. DOI: 10.1039/c7ta09427b.

(14) Nowroozi, M. A.; Wissel, K.; Donzelli, M.; Hosseinpourkahvaz, N.; Plana-Ruiz, S.; Kolb, U.; Schoch, R.; Bauer, M.; Malik, A. M.; Rohrer, J.; et al. High cycle life all-solid-state fluoride ion battery with La_2NiO_{4+d} high voltage cathode. *Communications Materials* **2020**, *1* (1). DOI: 10.1038/s43246-020-0030-5.

(15) McCabe, E. E.; Greaves, C. Fluorine insertion reactions into pre-formed metal oxides. *Journal of Fluorine Chemistry* **2007**, *128* (4), 448-458. DOI: 10.1016/j.jfluchem.2006.11.008.

(16) Clemens, O.; Slater, P. R. Topochemical modifications of mixed metal oxide compounds by low-temperature fluorination routes. *Reviews in Inorganic Chemistry* **2013**, *33* (2-3), 105-117. DOI: 10.1515/revic-2013-0002.

(17) Slater, P. R. Poly(vinylidene Fluoride) as a reagent for the synthesis of K_2NiF_4-related inorganic oxide Fluorides. *Journal of Fluorine Chemistry* **2002**, *117*, 43-45. DOI: 10.1016/S0022-1139(02)00166-5.

(18) Kwak, B. S.; Do, J. Y.; Park, N. K.; Kang, M. Surface modification of layered perovskite Sr_2TiO_4 for improved CO_2 photoreduction with H_2O to CH_4. *Scientific Reports* **2017**, *7* (1), 16370. DOI: 10.1038/s41598-017-16605-w. Kato, H.; Kudo, A. Water Splitting into H_2 and O_2 on Alkali Tantalate Photocatalysts $ATaO_3$ (A = Li, Na, and K). *Journal of Physical Chemistry B* **2001**, *105*, 4285-4292. DOI: 10.1021/jp004386b. Chen, X. B.; Shen, S. H.; Guo, L. J.; Mao, S. S. Semiconductor-based Photocatalytic Hydrogen Generation. *Chemical Reviews* **2010**, *110* (11), 6503–6570. DOI: 10.1021/cr1001645. Iizuka, K.; Wato, T.; Miseki, Y.; Saito, K.; Kudo, A. Photocatalytic Reduction of Carbon Dioxide over Ag Cocatalyst-Loaded $ALa_4Ti_4O_{15}$ (A = Ca, Sr, and Ba) Using Water as a Reducing Reagent. *Journal of American Chemical Society* **2011**, *133*, 20863–20868. DOI: dx.doi.org/10.1021/ja207586e. Yugo

Miseki; Hideki Kato; Kudo, A. Water splitting into H_2 and O_2 over niobate and titanate photocatalysts with (111) plane-type layered perovskite structure. *Energy & Environmental Science* **2009**, *2*, 306–314. DOI: 10.1039/B818922F.

(19) Zhang;, X.; Huang;, D.; Xu;, K.; Xu;, D.; Liu;, F.; Zhang, S. Indium-Containing Visible-Light-Driven (VLD) Photocatalysts for Solar Energy Conversion and Environment Remediation. In *Semiconductor Photocatalysis - Materials, Mechanisms and Applications*, Cao, W. Ed.; IntechOpen, 2016; pp 343–364.

(20) Tang, J. W.; Zou, Z. G.; Ye, J. H. Effects of Substituting Sr^{2+} and Ba^{2+} for Ca^{2+} on the Structural Properties and Photocatalytic Behaviors of $CaIn_2O_4$. *Chemistry of Materials* **2004**, *16*, 1644-1649. DOI: 10.1021/cm0353815.

(21) Ye, J. H.; Zou, Z. G.; Oshikiri, M.; Matsushita, A.; Shimoda, M.; Imai, M.; Shishido, T. A novel hydrogen-evolving photocatalyst $InVO_4$ active under visible light irradiation. *Chemical Physics Letters* **2002**, *356*, 221–226. DOI: 10.1016/S0009-2614(02)00254-3. Tang, J.; Zou, Z.; Yin, J.; Ye, J. Photocatalytic degradation of methylene blue on $CaIn_2O_4$ under visible light irradiation. *Chemical Physics Letters* **2003**, *382* (1-2), 175-179. DOI: 10.1016/j.cplett.2003.10.062.

(22) Tarasova, N.; Animitsa, I.; Galisheva, A.; Korona, D. Incorporation and Conduction of Protons in Ca, Sr, Ba-Doped $BaLaInO_4$ with Ruddlesden-Popper Structure. *Materials* **2019**, *12* (10). DOI: 10.3390/ma12101668.

(23) *DIFFRAC.SUITE TOPAS V.6.0*; 2017. (accessed.

(24) Günzler;, H.; Gremlich, H.-U. *IR-Spektroskopie*; Wiley-VCH, 2003. Otto, A. Excitation of Nonradiative Surface Plasma Waves in Silver by the Method of Frustrated Total Reflection. *Zeitschrift ffir Physik* **1968**, *216*, 398-410. DOI: 10.1007/BF01391532.

(25) Plana-Ruiz, S.; Krysiak, Y.; Portillo, J.; Alig, E.; Estrade, S.; Peiro, F.; Kolb, U. Fast-ADT: a fast and automated electron diffraction tomography setup for structure determination and refinement. *Ultramicroscopy* **2020**, *211*, 112951. DOI: 10.1016/j.ultramic.2020.112951.

(26) Kolb;, U.; Krysiak;, Y. a.; Plana-Ruiz, S. Automated electron diffraction tomography – development and applications. *Acta Crystallogr B Struct Sci Cryst Eng Mater* **2019**, *B75*, 463–474. DOI: 10.1107/S2052520619006711.

(27) Burla, M. C.; Caliandro, R.; Carrozzini, B.; Cascarano, G. L.; Cuocci, C.; Giacovazzo, C.; Mallamo, M.; Mazzone, A.; Polidori, G. Crystal structure determination and refinement *via SIR2014*. *Journal of Applied Crystallography* **2015**, *48*, 306–309. DOI: 10.1107/S1600576715001132.

(28) Petříček, V.; Dušek, M.; Palatinus, L. Crystallographic Computing System JANA2006: General features. *Zeitschrift für Kristallographie* **2014**, *229* (5), 345–352. DOI: 10.1515/zkri-2014-1737.

(29) Rovezzi, M.; Harris, A.; Detlefs, B.; Bohdan, T.; Svyazhin, A.; Santambrogio, A.; Degler, D.; Baran, R.; Reynier, B.; Noguera Crespo, P.; et al. TEXS: in-vacuum tender X-ray emission spectrometer with 11 Johansson crystal analyzers. *J Synchrotron Radiat* **2020**, *27*, 813-826. DOI: 10.1107/S160057752000243X.

(30) Escobedo Morales, A.; Sánchez Mora, E.; Pal, U. Use of diffuse reflectance spectroscopy for optical characterization of un-supported nanostructures. *REVISTA MEXICANA DE FISICA S* **2007**, *53* (3), 18–22.

(31) Brown;, I. D.; Altermatt, D. Bond-Valence Parameters Obtained from a Systematic Analysis of the Inorganic Crystal Structure Database. *Acta Crystallographica* **1985**, *B41*, 244-247. DOI: 10.1107/S0108768185002063.

(32) Salinas-Sanchez;, A.; Garcia-Muñoz;, J.; Rodriguez-Carvajal;, J.; Saez-Puche;, R.; Martinez, J. Structural Characterization of R_2BaCuO_5 (R = Y, Lu, Yb, Tm, Er, Ho, Dy, Gd, Eu

and Sm) Oxides by X-Ray and Neutron Diffraction. *Journal of Solid State Chemistry* **1992**, *100*, 201-211. DOI: 10.1016/0022-4596(92)90094-C.

(33) Chen;, H.; Wong;, L. L.; Adams, S. *SoftBV* – a software tool for screening the materials genome of inorganic fast ion conductors. *Acta Crystallographica* **2019**, *B75*, 18–33. DOI: 10.1107/S2052520618015718. Chen;, H.; Adams, S. Bond softness sensitive bond-valence parameters for crystal structure plausibility tests. *IUCrJ* **2017**, *4*, 614–625. DOI: 10.1107/S2052252517010211.

(34) Brese;, N. E.; O'Keefee, M. Bond-Valence Parameters for Solids. *Acta Crystallographica* **1991**, *B47*, 192-197. DOI: 10.1107/S0108768190011041.

(35) Blöchl, P. E. Projector augmented-wave method. *Physical Review B* **1994**, *50*, 17953 DOI: 10.1103/PhysRevB.50.17953.

(36) Kresse;, G.; Furthmüller, J. Efficient iterative schemes for ab initio total-energy calculations using a plane-wave basis set. *Physical Review B* **1996**, *54*, 11169. DOI: 10.1103/PhysRevB.54.11169. Kresse;, G.; Furthmüller, J. Efficiency of ab-initio total energy calculations for metals and semiconductors using a plane-wave basis set. *Computational Materials Science* **1996**, *6*, 15-50. DOI: 10.1016/0927-0256(96)00008-0. Kresse;, G.; Joubert, D. From ultrasoft pseudopotentials to the projector augmented-wave method. *Physical Review B* **1999**, *59*, 1758. DOI: 10.1103/PhysRevB.59.1758.

(37) Perdew;, J. P.; Burke;, K.; Ernzerhof, M. Generalized Gradient Approximation Made Simple. *Physical review Letters* **1996**, *77*, 3865. DOI: 10.1103/PhysRevLett.77.3865.

(38) Heyd;, J.; Scuseria, G. E. Assessment and validation of a screened Coulomb hybrid density functional. *Journal of Chemical Physics* **2004**, *120*, 7274. DOI: 10.1063/1.1668634. Heyd;, J.; Scuseria, G. E. Efficient hybrid density functional calculations in solids: Assessment of the Heyd–Scuseria–Ernzerhof screened Coulomb hybrid functional. *Journal of Chemical Physics* **2004**, *121*, 1187 DOI: 10.1063/1.1760074. Heyd;, J.; Scuseria;, G. E.; Ernzerhof, M. Hybrid

functionals based on a screened Coulomb potential. *The Journal of Chemical Physics* **2006**, *124*, 219906. DOI: 10.1063/1.2204597.

(39) Krukau;, A. V.; Vydrov;, O. A.; Izmaylov;, A. F.; Scuseria, G. E. Influence of the exchange screening parameter on the performance of screened hybrid functionals. *The Journal of Chemical Physics* **2006**, *125*, 224106 DOI: 10.1063/1.2404663.

(40) Blöchl;, P. E.; Jepsen;, O.; Andersen, O. K. Improved tetrahedron method far Brilleuin-zane integratians. *Physical Review B* **1994**, *49*, 16223 DOI: 10.1103/PhysRevB.49.16223.

(41) Clemens, O. Synthese und Charakterisierung von lithiumhaltigen Übergangsmetall-Phosphaten und –Vanadaten sowie von deren Mischkristallen. der Universität des Saarlandes, 2011.

(42) Shannon, R. D. Revised Effective Ionic Radii and Systematic Studies of Interatomie Distances in Halides and Chaleogenides. *Acta Crystallographica* **1976**, *A32*, 751-767. DOI: 10.1107/S0567739476001551.

(43) Tarasova, N.; Animitsa, I. Materials $A^{II}LnInO_4$ with Ruddlesden-Popper Structure for Electrochemical Applications: Relationship between Ion (Oxygen-Ion, Proton) Conductivity, Water Uptake, and Structural Changes. *Materials* **2021**, *15* (1). DOI: 10.3390/ma15010114. Tyitov, Y. O.; Byilyavina, N. M.; Markyiv, V. Y.; Slobodyanik, M. S.; Krajevs'ka, Y. A. Synthesis and crystal structure of $BaLaInO_4$ and $SrLnInO_4$ (Ln-La, Pr). *Dopovyidyi Natsyional'noyi Akademyiyi Nauk Ukrayini* **2009**, *10*, 160-166.

(44) Berry;, F. J.; Moore;, E.; Mortimer;, M.; Ren;, X.; Heap;, R.; Slater;, P.; Thomas, M. F. Synthesis and structural investigation of a new oxide fluoride of composition $Ba_2SnO_{2.5}F_3 \cdot xH_2O$ (x≈0.5). *Journal of Solid State Chemistry* **2008**, *181*, 2185–2190. DOI: 10.1016/j.jssc.2008.05.015. Slater;, P. R.; Gover, R. K. B. Synthesis and structure of the new oxide fluoride $Ba_2ZrO_3F_2 \cdot xH_2O$ (x≈0.5). *Journal of Materials Chemistry* **2001**, *11*, 2035–2038. DOI: 10.1039/b103891p.

(45) Wissel, K.; Heldt, J.; Groszewicz, P. B.; Dasgupta, S.; Breitzke, H.; Donzelli, M.; Waidha, A. I.; Fortes, A. D.; Rohrer, J.; Slater, P. R.; et al. Topochemical Fluorination of La_2NiO_{4+d}: Unprecedented Ordering of Oxide and Fluoride Ions in $La_2NiO_3F_2$. *Inorganic Chemistry* **2018**, *57* (11), 6549-6560. DOI: 10.1021/acs.inorgchem.8b00661.

(46) Wissel, K.; Malik, A. M.; Vasala, S.; Plana-Ruiz, S.; Kolb, U.; Slater, P. R.; da Silva, I.; Alff, L.; Rohrer, J.; Clemens, O. Topochemical Reduction of $La_2NiO_3F_2$: The First Ni-Based Ruddlesden–Popper n = 1 T′-Type Structure and the Impact of Reduction on Magnetic Ordering. *Chemistry of Materials* **2020**, *32* (7), 3160-3179. DOI: 10.1021/acs.chemmater.0c00193.

(47) Jacobs;, J.; Marques;, M. A. L.; Wang;, H.-C.; Dieterich;, E.; Ebbinghaus, S. G. Structure, Magnetism, and Thermal Stability of $La_2NiO_{2.5}F_3$:A Ruddlesden−Popper Oxyfluoride Crystallizing in Space Group $P4_2/nnm$. *Inorganic Chemistry* **2021**, *60*, 13646−13657. DOI: 10.1021/acs.inorgchem.1c01957.

(48) Needs, R. L.; Weller, M. T. Synthesis and Structure of Ba_2InO_3F: Oxide/Fluoride Ordering in a New K_2NiF_4 Superstructure. *Journal of the Chemical Society, Chemical Communications* **1996**, *6* (7), 1219-1224. DOI: 10.1039/C39950000353. Needs, R. L.; Weller, M. T.; Schelerb, U.; K., H. R. Synthesis and structure of Ba_2InO_3X (X = F, Cl, Br) and Ba_2ScO_3F oxidehalide ordering in K_2NiF_4-type structures. *Journal of Materials Chemistry* **1996**, *6* (7), 1219-1224. DOI: 10.1039/JM9960601219.

(49) Ebrahimizadeh Abrishami, M.; Risch, M.; Scholz, J.; Roddatis, V.; Osterthun, N.; Jooss, C. Oxygen Evolution at Manganite Perovskite Ruddlesden-Popper Type Particles: Trends of Activity on Structure, Valence and Covalence. *Materials* **2016**, *9* (11). DOI: 10.3390/ma9110921.

(50) Jacobs;, J.; Hester;, J. R.; Ebbinghaus, S. G. Cuprate Oxyfluorides $La_2Cu_{0.8}Ni_{0.2}O_3F_2$ and $La_2CuO_3F_2$ with "Channel-like" Anion Ordering. *Inorganic Chemistry* **2022**, *61*, 17202−17211. DOI: 10.1021/acs.inorgchem.2c02776.

(51) Xu, Q. C.; Wellia, D. V.; Ng, Y. H.; Amal, R.; Tan, T. T. Y. Synthesis of Porous and Visible-Light Absorbing Bi_2WO_6/TiO_2 Heterojunction Films with Improved Photoelectrochemical and Photocatalytic Performances. *The Journal of Physical Chemistry C* **2011**, *115* (15), 7419-7428. DOI: 10.1021/jp1090137.

(52) Yu;, J.; Wang;, W.; Cheng;, B.; Su, B.-L. Enhancement of Photocatalytic Activity of Mesporous TiO_2 Powders by Hydrothermal Surface Fluorination Treatment. *Journal of Physical Chemistry C* **2009**, *113*, 6743–6750. DOI: 10.1021/jp900136q

(53) Wang;, S.; Huang;, B.; Wang;, Z.; Liu;, Y.; Wei;, W.; Qin;, X.; Zhang;, X.; Dai, Y. A new photocatalyst: $Bi_2TiO_4F_2$ nanoflakes synthesized by a hydrothermal method. *Dalton Transactions* **2011**, *40*, 12670. DOI: 10.1039/c1dt10889a.

(54) Kuriki;, R.; Ichibha;, T.; Hongo;, K.; Lu;, D.; Maezono;, R.; Kageyama;, H.; Ishitani;, O.; Oka;, K.; Maeda, K. A Stable, Narrow-Gap Oxyfluoride Photocatalyst for Visible-Light Hydrogen Evolution and Carbon Dioxide Reduction. *Journal of American Chemical Society* **2018**, *140*, 6648−6655. DOI: 10.1021/jacs.8b02822.

(55) Rahal;, R.; Wankhade;, A.; Cha;, D.; Fihri;, A.; Ould-Chikh;, S.; Patil;, U.; Polshettiwar, V. Synthesis of hierarchical anatase TiO_2 nanostructures with tunable morphology and enhanced photocatalytic activity. *RSC Advances* **2012**, *2*, 7048–7052. DOI: 10.1039/ c2ra21104a.

(56) Perween;, S.; Wissel;, K.; Dallos;, Z.; Weiss;, M.; Vasala;, S.; Strobel;, S.; Schuetzenduebe;, P.; Kolb;, U.; Marschall;, R.; Glatzel, P. Improving the Photocatalytic activity for Hydrogen Evolution of $LaBaInO_4$ via Topochemical Fluorination to $LaBaInO_3F_2$.

In *ChemRxiv. Cambridge: Cambridge Open Engage; This content is a preprint and has not been peer-reviewed. DOI: 10.26434/chemrxiv-2022-0dnsz*, 2022.

For Table of Contents Only

■ SYNOPSIS

A non-oxidative topochemical fluorination of $LaBaInO_4$ to $LaBaInO_3F_2$ were successfully obtained which shows a strong expansion perpendicular to the perovskite layers, accompanied by a strong tilting of the octahedra in the *ab* plane. The structural impact on the optical properties has been studied. Additionally, we provide the *ab initio* density functional theory (DFT) calculations in support of the structural-optical properties obtained experimentally. Both the compounds, oxide as well oxyfluoride, show photocatalytically active for H_2 evolution.

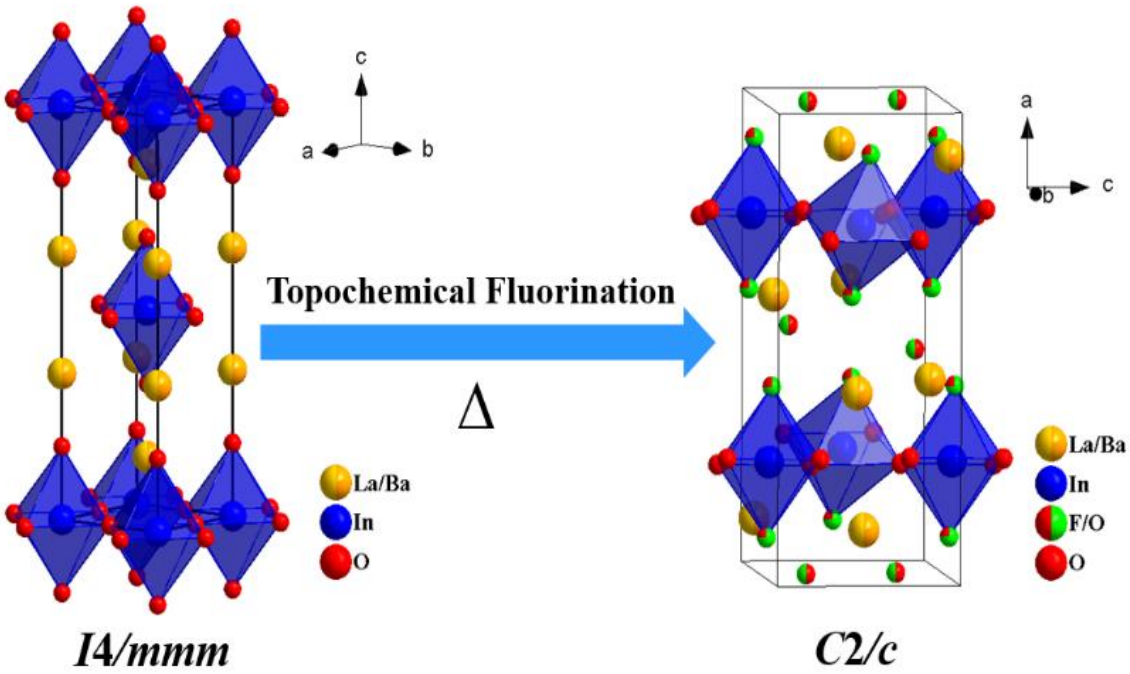

Graphical Abstract: *Crystal structure of $LaBaInO_4$ and $LaBaInO_3F_2$.*